# High-Resolution Simulation of Hurricane Bonnie (1998). Part I: The Organization of Eyewall Vertical Motion

SCOTT A. BRAUN

*Mesoscale Atmospheric Processes Branch, Laboratory for Atmospheres, NASA Goddard Space Flight Center, Greenbelt, Maryland*

MICHAEL T. MONTGOMERY

*Department of Atmospheric Science, Colorado State University, Fort Collins, Colorado*

ZHAOXIA PU

*Department of Meteorology, University of Utah, Salt Lake City, Utah*

(Manuscript received 7 November 2003, in final form 8 October 2004)

ABSTRACT

The fifth-generation Pennsylvania State University–National Center for Atmospheric Research (PSU–NCAR) Mesoscale Model (MM5) is used to simulate Hurricane Bonnie at high resolution (2-km spacing) in order to examine how vertical wind shear impacts the distribution of vertical motion in the eyewall on both the storm and cloud scale. As in many previous studies, it is found here that the shear produces a wavenumber-1 asymmetry in the time-averaged vertical motion and rainfall. Several mechanisms for this asymmetry are evaluated. The vertical motion asymmetry is qualitatively consistent with an assumed balance between horizontal vorticity advection by the relative flow and stretching of vorticity, with relative asymmetric inflow (convergence) at low levels and outflow (divergence) at upper levels on the downshear side of the eyewall. The simulation results also show that the upward motion portion of the eyewall asymmetry is located in the direction of vortex tilt, consistent with the vertical motion that required to maintain dynamic balance. Variations in the direction and magnitude of the tilt are consistent with the presence of a vortex Rossby wave quasi mode, which is characterized by a damped precession of the upper vortex relative to the lower vortex.

While the time-averaged vertical motion is characterized by ascent in a shear-induced wavenumber-1 asymmetry, the instantaneous vertical motion is typically associated with deep updraft towers that generally form on the downtilt-right side of the eyewall and dissipate on the downtilt-left side. The updrafts towers are typically associated with eyewall mesovortices rotating cyclonically around the eyewall and result from an interaction between the shear-induced relative asymmetric flow and the cyclonic circulations of the mesovortices. The eyewall mesovortices may persist for more than one orbit around the eyewall and, in these cases, can initiate multiple episodes of upward motion.

## 1. Introduction

Early studies of the asymmetric structure of tropical cyclones found that the maximum precipitation tended to occur in the front quadrants relative to the storm motion. Several of these cases involved storms near coasts, so land influences may have played a role. Marks (1985) examined a case over the open ocean and also found a tendency for the maximum precipitation to occur in the front quadrants. It was suggested that this pattern of precipitation is caused by the effects of boundary layer friction associated with a translating hurricane. Shapiro (1983), using a slab boundary layer model, showed that a translating storm develops asymmetries in the pattern of frictional convergence within the boundary layer such that the maximum convergence occurs in front of the storm.

More recent studies have demonstrated an important influence of environmental vertical wind shear on the asymmetric structure of hurricanes. Corbosiero and Molinari (2003) used lightning data as a proxy for ver-

*Corresponding author address:* Dr. Scott A. Braun, Mesoscale Atmospheric Processes Branch, Laboratory for Atmospheres, NASA GSFC, Code 613.1, Greenbelt, MD 20771.
E-mail: Scott.A.Braun@nasa.gov

© 2006 American Meteorological Society

tical motion in an examination of tropical cyclones ranging from depressions to tropical storms to hurricanes. They found that lightning occurrence showed a marked downshear tendency that increased with the strength of the shear. In the inner core, storms in environments with shear[1] less than 10 m $s^{-1}$ exhibited little left–right preference relative to the shear vector, but for stronger shear, a clear left signal was present. For the outer bands, in moderate to strong shear (>5 m $s^{-1}$), there was a clear downshear-right signal. These relationships held irrespective of storm intensity or of the underlying surface (land or ocean).

Several mechanisms have been proposed by which vertical shear produces asymmetries in vertical motions in adiabatic vortices. This shear can be associated with the environmental winds or with beta gyres caused by the advection of planetary vorticity by the hurricane vortex (Wang and Holland 1996a; Bender 1997). Bender (1997) showed that the weakening of beta gyres with height can produce vertical shear on the order of 5 m $s^{-1}$ over the depth of the troposphere.

One mechanism for generating asymmetric vertical motion is related to the tilting of the vortex by the vertical shear (Raymond 1992; Jones 1995; Wang and Holland 1996a; Frank and Ritchie 1999). In order for the vortex to remain balanced, the isentropes must be raised in the direction of tilt and lowered on the other side, that is, a negative potential temperature anomaly occurs downtilt and a positive anomaly uptilt. This effect is accomplished by upward (downward) motion on the downtilt (uptilt) side of the vortex. Jones (1995), Wang and Holland (1996a,c), and Frank and Ritchie (1999) showed that this mechanism is only active for a brief period after tilting of the adiabatic vortex, after which time a second mechanism becomes important. Since the temperature anomaly is fixed with respect to the vortex tilt, the second mechanism for vertical motion occurs as the vortex flow moves adiabatically through the temperature anomalies (Jones 1995). Upward motion occurs as the air moves from the positive to the negative temperature anomalies and downward motion occurs as air moves from the negative to the positive anomalies. Consequently, the vertical motion is 90° out of phase with the temperature anomalies with the upward motion to the right of the direction of vortex tilt. Note that the location of upward motion is described in relation to the tilt direction rather than the direction of shear. In many cases, the directions of tilt and shear may be different as a result of the mutual interaction and corotation of the upper- and lower-level vortices (Jones 1995; Reasor and Montgomery 2001; Reasor et al. 2004).

Wang and Holland (1996b,c), Bender (1997), and Frank and Ritchie (1999, 2001) have shown that, whether the shear comes from the environmental flow or from the beta gyres, the upward motion part of the asymmetry in a diabatic vortex usually occurs downshear or slightly downshear-left while the precipitation is typically left of the shear. A proposed mechanism for the downshear maximum in upward motion in diabatic vortices is related to the relative flow within the vortex (Willoughby et al. 1984; Bender 1997; Frank and Ritchie 2001). If the vortex moves with the ambient flow at a particular level, called the steering level, then there will be flow relative to the vortex above and below the steering level. The hurricane inner core is a region of high vorticity with strong vorticity gradients near the eyewall. Conservation of vorticity suggests that strong vorticity advection must be approximately balanced by stretching or compression of vorticity. As a result, where the relative flow is directed inward (outward), the negative (positive) vorticity advection is balanced by vortex stretching (shrinking) associated with convergence (divergence). For a vortex in unidirectional shear, low-level inflow and upper-level outflow occur on the downshear side of the vortex, thereby producing low-level convergence and upper-level divergence and a deep layer of upward vertical motion. The opposite occurs on the upshear side of the vortex.

Diabatic vortices generally have much smaller tilts than their adiabatic counterparts, usually much less than the radius of maximum winds. It has been argued that the diabatic heating associated with convection opposes the tilting by more strongly coupling the lower and upper vortices (Wang and Li 1992; Flatau et al. 1994; Wang and Holland 1996c). Reasor et al. (2004) have argued that the moist dynamics associated with diabatic vortices are not fundamentally different than the adiabatic dynamics. They showed that, as long as the shear is not too strong, adiabatic vortices are quite resilient to shear. They examined the tilting of a vortex by shear and found that a damping mechanism intrinsic to the dry adiabatic dynamics suppresses departures from an upright state. This realignment occurs through projection of the tilt asymmetry onto two types of vortex Rossby waves: a quasi mode, or discrete, vortex Rossby wave that causes long-lived precession of the upper part of a tilted vortex relative to the lower part, and sheared vortex Rossby waves in which the radial shear of the swirling flow axisymmetrizes tilt asymmetries, resulting in short-lived precession and more rapid

[1] They computed the wind shear between 850 and 200 hPa by averaging winds from ECMWF analyses over a circle of 500-km radius centered on the storm.

reduction of the tilt. They suggested that the effects of moisture simply enhance this process.

Black et al. (2002) described the structure of eastern Pacific Hurricanes Jimena (1991) and Olivia (1994) using aircraft radar and flight-level in situ data. Jimena was able to maintain category 4 intensity despite estimated vertical shear of 13–20 m $s^{-1}$ while Olivia strengthened in 8 m $s^{-1}$ shear. In both cases, shear produced a wavenumber-1 distribution of convection with the highest reflectivities in the semicircle to the left of the shear direction. The convective cells comprising this reflectivity asymmetry were periodic, with echoes forming on the downshear side of the eyewall, growing and maturing on the left side of the shear vector, and often dissipating on the upshear side. In some cases, clusters of cells were observed to move around the eyewall multiple times, initiating new bursts of convection as they moved again into the downshear portion of the eyewall. The cells typically moved more slowly than the mean flow near the radius of maximum wind, consistent with the behavior of vortex Rossby waves (Montgomery and Kallenbach 1997; Chen and Yau 2001; Fulton 2001).

This study examines a high-resolution simulation of Hurricane Bonnie (1998) using the fifth-generation Pennsylvania State University–National Center for Atmospheric Research (PSU–NCAR) Mesoscale Model (MM5) for the purpose of examining the impact of vertical shear on the distribution of vertical motion in the eyewall. Rogers et al. (2003) and Zhu et al. (2004) have previously simulated Bonnie using MM5 and have described various aspects regarding the impact of shear on wavenumber-1 asymmetries. Rogers et al. (2003) showed that the accumulated rainfall was distributed symmetrically across the storm track when the shear was directed across track, while it was distributed asymmetrically when the shear was directed along the track. Zhu et al. (2004) described the interaction of Bonnie with an approaching upper trough and suggested that storm-relative flow associated with the trough moving into the storm core produced upper-level convergence and downward motion that suppressed convection on the upshear side of the eyewall. Both studies described a relationship between vortex tilt and upward motion on the downtilt side of the eyewall. In this study, we further evaluate the relationship between vortex tilt and wavenumber-1 vertical motion asymmetries and describe the behavior of the tilt evolution in terms of the shear-induced relative flow and the modeling results of Reasor et al. (2004).

Heymsfield et al. (2001) described the structure of Hurricane Bonnie on 23 August 1998, using multiple observations from the National Aeronautics and Space Administration (NASA) Convection and Moisture Experiment (CAMEX-3). Observations from the NASA ER-2 Doppler radar indicated isolated deep convective towers on the eastern side of the storm with updrafts greater than 10 m $s^{-1}$. Heymsfield et al. (2001) developed a conceptual model for the evolution of the convective towers in which the updrafts formed near the top of the boundary layer on the southern (downshear right) side of the eyewall and grew progressively taller while moving around to the northern (downshear left) side. In other words, the convection was viewed in terms of rising plumes of air that were initiated to the south and reached the upper troposphere to the north of the eye. We go beyond previous studies (Rogers et al. 2003; Zhu et al. 2004) and examine the processes controlling the timing and location of individual updrafts and relate these findings, and those of Black et al. (2002), to the vorticity dynamics of the eyewall. The results will also be compared to the conceptual model of Heymsfield et al. (2001) to determine the extent to which this conceptual model explains vertical motions and precipitation growth in the eyewall of the simulated storm.

Section 2 provides a brief overview of Bonnie's evolution, its precipitation structure as measured by the NASA Tropical Rainfall Measurement Mission (TRMM) satellite, and the relationship between the storm's structure and intensity changes to the evolution of the vertical shear. Section 3 summarizes the numerical model configuration, physics options, and initial conditions, as well as provides some basic validation of the numerical simulation. Section 4 describes the time-averaged structure and describes the relationship between the simulated wavenumber-1 asymmetry in vertical motion and the vertical wind shear. Section 5 examines the time-varying structure of the eyewall vertical motions and the role that eyewall mesovortices play in determining the timing and location of updrafts. Finally, conclusions are provided in section 6.

## 2. Synoptic discussion

A very brief description of Bonnie's evolution is provided here. See Pasch et al. (2001), Rogers et al. (2003), and Zhu et al. (2004) for more complete summaries. The environmental vertical shear discussed below is determined following Kaplan and DeMaria (2003) from the difference between the 850- and 200-hPa wind vectors averaged between 200- and 800-km radius. Two estimates are provided: one from the European Centre for Medium-Range Weather Forecasts (ECMWF) large-scale analyses and one from the Statistical Hurricane Intensity Prediction Scheme (SHIPS) model database, derived from the National Centers for Environmental Prediction (NCEP) reanalysis. The analyses

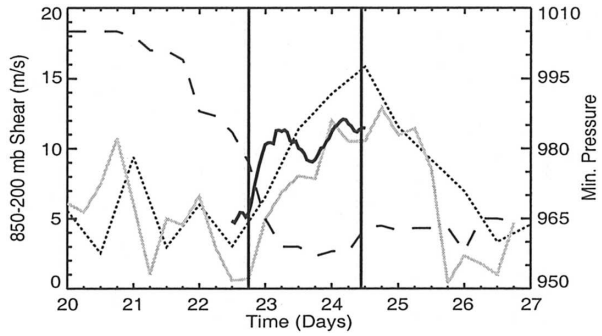


FIG. 1. Time series of the large-scale 850–200-mb vertical wind shear and minimum sea level pressure. Wind shear information was obtained by averaging wind fields between radii of 200 and 800 km: ECMWF, light solid line; SHIPS (NCEP) reanalysis data, dotted line; MM5, dark solid line. Minimum sea level pressure (dashed line) was obtained from best-track estimates. Vertical lines indicate the times of the TRMM overpasses.

produce very similar variations of the large-scale shear (Fig. 1).

Bonnie formed as a tropical depression at 1200 UTC 19 August and slowly developed into a tropical storm by 1200 UTC 20 August and into a hurricane by 0000 UTC 22 August. During this development period, the storm was embedded in generally southeasterly flow with weak-to-moderate shear (Fig. 1). On 22 August, the shear diminished and the storm rapidly intensified. Radar reflectivity data from the TRMM precipitation radar during an overpass at 1800 UTC 22 August (Fig. 2a) showed a well-defined eyewall with heavy precipitation concentrated on the northern and southeastern portions of the eyewall and multiple convective rainbands and broad stratiform precipitation generally to the north and east of the center. While not symmetric in structure, precipitation surrounded much of the storm center.

Between 22 and 24 August, Bonnie approached a weak, nearly stationary upper-level trough over the southeastern United States. Upper-level storm-relative flow switched from southeasterly to northwesterly and the vertical wind shear increased significantly. Concomitantly, further intensification of Bonnie was halted (Fig. 1). By 24 August, westerly flow at 200 hPa associated with the trough clearly impinged on the western side of the storm (see Fig. 10 of Zhu et al. 2004). The increased shear led to a highly asymmetric precipitation structure (Fig. 2b) with precipitation concentrated primarily to the east of the center while the storm's intensity remained relatively constant. Upon relaxation of the shear and a return to southerly flow on 25 August, Bonnie began to move more rapidly to the northwest. Bonnie subsequently underwent an eyewall replacement cycle (Rogers et al. 2003; Zhu et al. 2004) prior to making landfall in North Carolina late on 26 August.

## 3. Simulation description and validation

### *a. Model description*

The model used in this study is the nonhydrostatic PSU–NCAR MM5 (version 3.4; Dudhia 1993; Grell et al. 1995). Because of computational limitations, the simulation was conducted in two steps. First, a coarse-resolution simulation was performed using an outer mesh (Fig. 3) with 36-km horizontal grid spacing, 91 × 97 grid points in the $x$ and $y$ directions, respectively, and

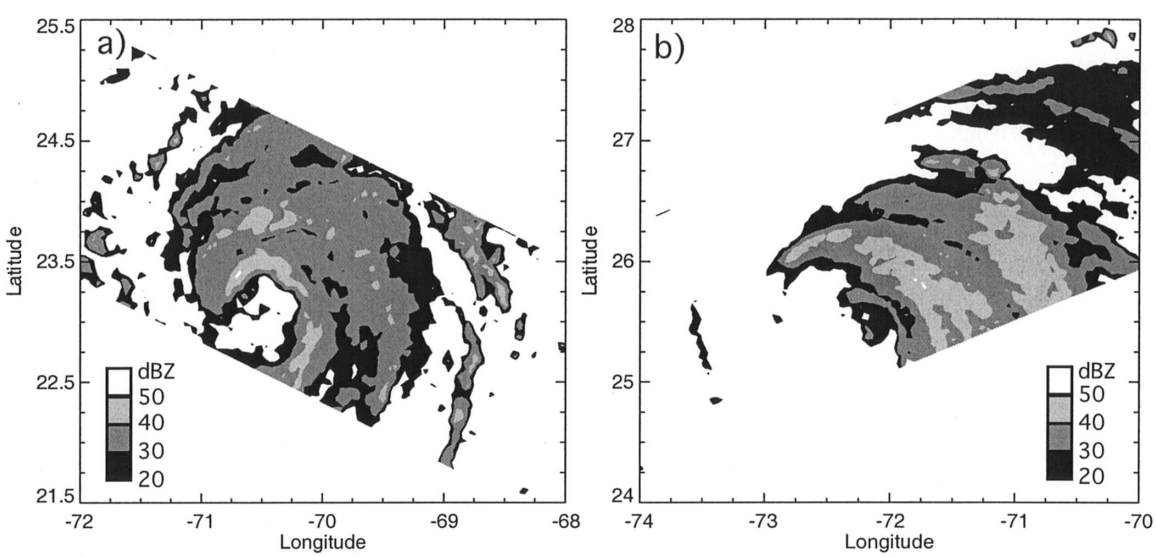


FIG. 2. Radar reflectivity at 2 km MSL from the TRMM precipitation radar for (a) 1800 UTC 22 Aug and (b) 1050 UTC 24 Aug.

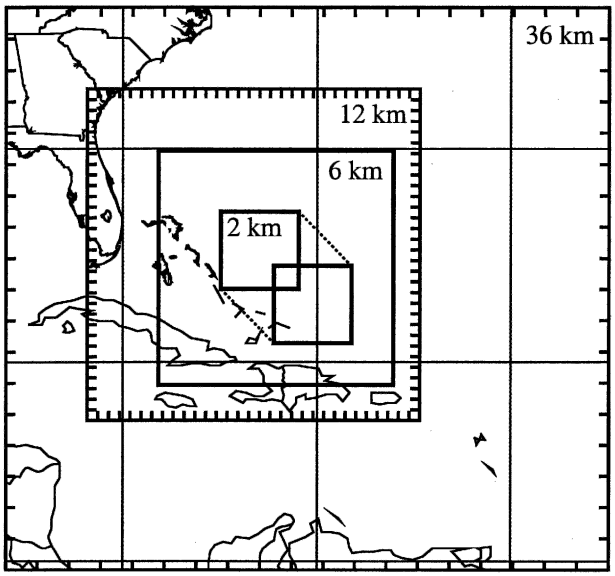


FIG. 3. Map of the coarse- and fine-mesh domains. The finest 2-km grid is moved with the storm, but only its initial and final positions are shown. Tick marks for the outer 36-km grid and inner 12-km grid are drawn every five grid points.

27 vertical levels. A second inner mesh with 12-km horizontal grid spacing consisted of 160 × 160 grid points. The simulation was started at 1200 UTC 22 August 1998 and run for 36 h, with model output saved every hour. Physics options for the coarse grid simulation included a modified version of the Blackadar planetary boundary layer scheme in which surface roughness calculations for momentum, temperature, and moisture follow Garratt (1992) and Pagowski and Moore (2001). Cloud processes were represented by the Grell cumulus parameterization scheme and the Goddard Cumulus Ensemble model cloud microphysics. Shortwave radiative processes were represented by the cloud-radiation scheme of Dudhia (1989) while longwave radiation used the Rapid Radiative Transfer Model (RRTM) of Mlawer et al. (1997) and were calculated every five minutes. Although heating associated with the dissipation of turbulent kinetic energy near the surface has been shown to have an impact on hurricane intensity (Bister and Emanuel 1998; Zhang and Altshuler 1999), this effect has not been included in this study.

Initial and boundary conditions were obtained from 12-hourly global analyses from the ECMWF archived at NCAR. Analysis fields, including temperature, relative humidity, geopotential height, and winds at mandatory pressure levels and with horizontal resolution of 2.5° were interpolated horizontally to model grid points. These interpolated analyses were refined by adding information from standard twice-daily rawinsondes and three-hourly surface and buoy reports using a Barnes objective analysis technique (Manning and Haagenson 1992). Final analyses were then interpolated to the model vertical levels. Sea surface temperatures were taken from NCEP analyses and were held fixed during the simulation.

Because the large-scale analysis did not contain an adequate representation of the initial hurricane vortex, a bogusing technique using four-dimensional variational data assimilation developed by Zou and Xiao (2000) and Xiao et al. (2000) and modified by Pu and Braun (2001) was used. See Pu and Braun (2001) for a complete description of the methodology. The assimilation was performed on the 36-km grid only. A bogus sea level pressure field was specified using the analytic profiles proposed by Holland (1980) while the tangential winds were derived by assuming gradient wind balance. Bogus winds above the surface were obtained by multiplying the surface wind values by an empirical function, as suggested in Kurihara et al. (1993), that decreased with height from a value of 1 in the boundary layer to zero above about 200 hPa. The values of central sea level pressure, maximum wind speed, and radius of maximum wind (RMW) prescribed for the bogus vortex were 980 hPa, 37.5 m $s^{-1}$, and 120 km, respectively. Pu and Braun (2001) found that use of a larger than observed radius of maximum wind produced better results because the 36-km grid was incapable of resolving the structure of the eye when the observed radius (about 40 km in this case) was used. Because of the coarse resolution, the initial grid value of the central pressure is somewhat higher than the prescribed value.

A high-resolution simulation was conducted by using 1-h output from the 36- and 12-km grids to provide initial and boundary conditions for a 6-km grid (225 × 225 × 27 grid points) and 2-km grid (226 × 226 × 27) starting at 6 h into the forecast to allow for some model spin up on the 12-km grid. The high resolution grids were run for 30 h until 0000 UTC 24 August. The 2-km grid was moved hourly to keep it centered on the storm. Model physics were identical to the coarse grid simulation except that no cumulus parameterization scheme was used and model output was saved every 15 min. The high resolution simulation was repeated for the period between 24 and 30 h (1200–1800 UTC 23 August) with model output every 3 min in order to resolve the evolution of individual updrafts.

For most applications, including computation of storm motion and compositing of output fields to a storm-relative grid, the storm center was determined, as in Braun (2002), at every model output time using the pressure field at the lowest model level. The horizontal distribution of pressure was used to determine an ap-

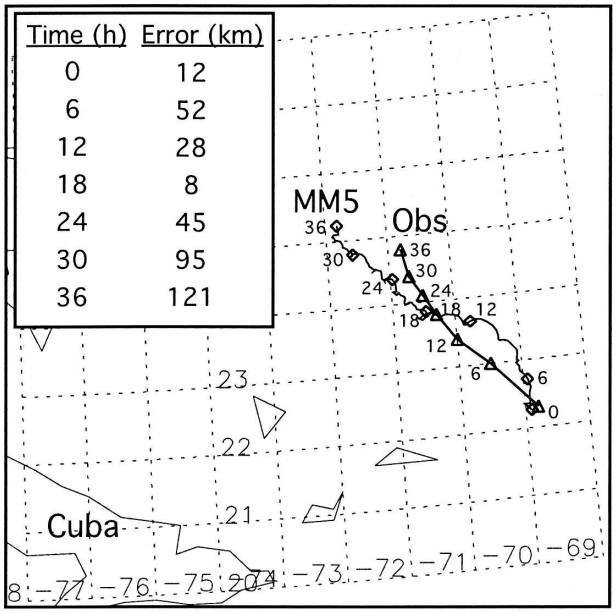


FIG. 4. Comparison of the observed (solid line with triangles) and simulated (diamonds) tracks. Symbols are drawn at 6-h intervals starting at 1200 UTC 22 Aug. Numerical values of track error are provided in the inset table. Time is indicated in terms of model hour.

proximate geometric center, or centroid, of the pressure field. The location of the minimum pressure was used as a first guess for the center. A variational approach was then used that adjusts the location of the center until the azimuthal variance of the pressure field at all radii between the center and the outer portion of the eyewall (100 km) was minimized. This methodology worked well not only for identifying the centroid of the pressure field but also the approximate centroid of the ring of strong tangential winds and vorticity. Storm motion was then computed from the identified center locations. To compute the time-averaged fields in section 4, model output fields at all heights were transferred to a grid in which the storm's surface center was fixed with respect to time.

### *b. Simulation validation*

In this section, we provide a basic validation of the simulated track, intensity, and precipitation structure. Figure 4 compares the simulated track to that observed. Because of the use of the bogus vortex, the initial error is very small and is approximately equal to the grid spacing of the second nest (12 km). During the first 18 h, the simulated storm track exhibits an eastward bias while in the following 18 h, the storm track exhibits a northwesterly bias relative to the observations. The track errors are comparable to those of Rogers et al. (2003) and somewhat smaller than those of Zhu et al. (2004).

The simulated intensity is depicted in Fig. 5 in terms of both the minimum sea level pressure and the maximum surface wind speed. Data from the first 6 h is obtained from the 12-km grid while information at later times is from the 2-km grid. The simulated minimum sea level pressure compares favorably with that observed since it is generally within 5–8 hPa of the observed value. During the first 24 h of simulation, the trend in the minimum sea level pressure also agrees well with observations, while in the last 12 h the simulated storm shows a greater deepening rate than observed.

The maximum simulated surface winds, estimated from the maximum wind speed at any grid point on the lowest model level, are shown in Fig. 5b and are compared to the estimated maximum surface winds measured within Bonnie by reconnaissance aircraft. The simulated maximum surface winds show intensification comparable to the observed rate during the first 6 h as

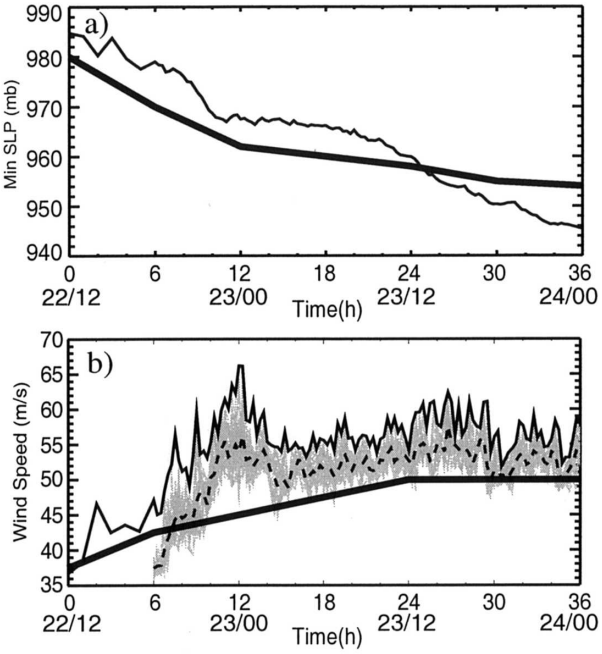


FIG. 5. Comparison of the observed (thick solid lines) and simulated (thin lines) intensity as measured by (a) the minimum sea level pressure and (b) the maximum surface wind speed. Results from the first 6 h are from the 12-km grid, and for the remainder of the simulation are from the 2-km grid. In (b), the thin solid line is the maximum wind speed at any grid point on the lowest model level from MM5, while the thick solid line is the observed maximum surface wind. The closely packed gray lines represent estimates of the simulated maximum wind from 121 hypothetical flight legs ranging from the northwest to the northeast of the center at each time, while the thin dashed line is the average of these estimates. Dates and times are provided along the horizontal axis along with model hour and denoted by date/time (UTC).

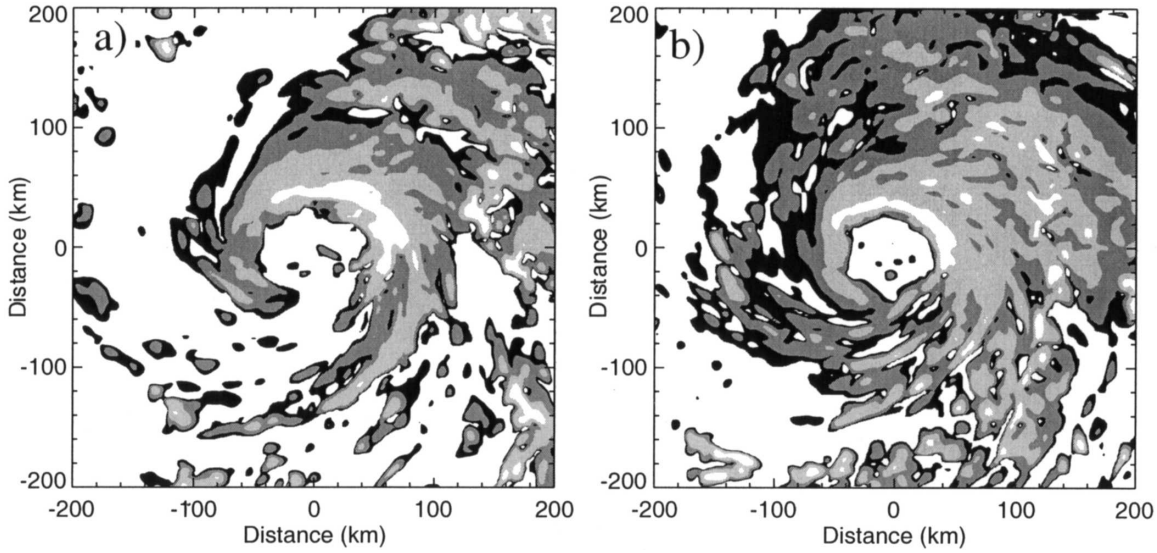


FIG. 6. Simulated radar reflectivity at 1 km MSL at (a) 18 and (b) 24 h. Shaded contours are drawn at 20, 30, 40, and 50 dB$Z$.

the storm initially develops on the 12-km grid and then a very rapid intensification between 6 and 12 h as the simulated storm adjusts to the increased resolution of the 2-km grid. By 14 h, the intensification associated with the spin up diminishes and thereafter the maximum surface winds exhibit a gradual intensification through 26 h and then a leveling off or slight decrease in the following hours. The simulated maximum surface winds after 14 h are generally 5–10 m s$^{-1}$ stronger than those observed. This result may be due, in part, to the limited sampling by the aircraft, which would not be expected to sample highly localized wind maxima. An estimate of the simulated maximum winds that is an analog to the flight data can be obtained from the model output as follows. Consider a series of hypothetical flight legs from the storm center through the region of the time-averaged maximum wind speed to the right of the storm motion, in this case on the northern to northeastern sides of the eyewall. The simulated wind speeds are interpolated to 121 hypothetical flight legs spanning this region and the maximum values at each time are determined. Time series of maximum wind obtained from these hypothetical flight legs are shown in Fig. 5b (gray lines). They show that for any given flight leg at any time, the maximum wind observed along the flight leg can be very close to the actual maximum or may be significantly less. The average profile (dashed line) suggests that a "typical" model flight leg would tend to underestimate the true maximum wind in the model by ~4–5 m s$^{-1}$. Using this average flight-leg value as a measure of the simulated intensity, a reduction of the intensity error by ~50% is seen for the period after 14 h. The results therefore indicate that the model maximum winds are consistently about 10% too strong. However, the trend in the wind speeds following the initial model spin up is generally good.

Figure 5 indicates that, after 24 h, the minimum sea level pressure continues to decrease while the maximum winds level off or weaken slightly. These results are not necessarily inconsistent. Idealized modeling of eyewall mesovortex formation and axisymmetrization by Schubert et al. (1999) and Kossin and Schubert (2001) suggests that the central pressure can decrease while the maximum winds decrease as a result of the potential vorticity redistribution by horizontal mixing. As vorticity is mixed into the eye, the peak winds at the RMW decrease, while the winds inside the RMW increase and the pressure decreases. The regular occurrence of mesovortices (section 5) in the current simulation may be an indication that a similar process is active here.

The simulated precipitation structure is shown in Fig. 6, where simulated radar reflectivity[2] fields are shown at 18 and 24 h (valid 0600 and 1200 UTC 23 August). At 18 h (Fig. 6a), 12 h into the 2-km grid simulation, in-

[2] The equivalent radar reflectivity factor for any hydrometeor category, $Z_x$, is computed following Fovell and Ogura (1988) as $Z_x = 720\alpha\kappa N_{0x}\lambda_x^{-7}(\rho_x/\rho_w)^2$, where $\alpha$ is the ratio of the backscattering coefficients for the reflecting particles and water (0.213 for snow and graupel, 1 for rain); $\kappa = 10^{18}$; $N_{0x}$ is the intercept parameter of the particle size distribution; $\lambda_x$ is the slope of the size distribution, $\lambda_x = (\pi\rho_x N_x/\rho q_x)^{1/4}$; $\rho$, $\rho_w$ and $\rho_x$ are the densities of air, water and the hydrometeor type (rain, snow, graupel), respectively; and $q_x$ is the hydrometeor mixing ratio. The reflectivity is expressed in decibels, or dB$Z$, where dB$Z = 10\log_{10}(Z_r + Z_s + Z_g)$.

tense precipitation is found on the northeastern side of the eyewall while a precipitation-free area occurs on the southern side. Outer convective rainbands are seen on the northeastern and eastern sides of the storm and very little stratiform precipitation occurs between the eyewall and the outer rainbands. By 24 h (Fig. 6b), the area of precipitation has increased as a significant amount of stratiform precipitation has developed. The heaviest eyewall precipitation remains on the northern and eastern sides of the eyewall. This structure is then maintained for the remainder of the simulation.

The simulated precipitation structure agrees well with that observed by TRMM during the low-shear period on 22 August (Fig. 2a), but is much less asymmetric than the observed storm during the high-shear period (Fig. 2b). This error may have several possible causes. One possibility is that the vertical shear in the simulation is too weak. However, shear values derived following Kaplan and DeMaria (2003) using output from the MM5 12-km grid show magnitudes comparable to the large-scale analyses (Fig. 1), suggesting that weak shear is not the cause. More likely causes are related to storm intensity and precipitation errors. The simulated tangential winds are somewhat too strong and may act to advect hydrometeors too far around the eyewall. In addition, the overall amount of precipitation appears to be too large (cf. Figs. 2 and 6), which would further contribute to excessive hydrometeor advection around to the western side of the storm. These problems themselves may have several causes including errors in the large-scale initial conditions, errors associated with the bogus vortex, and errors associated with the parameterized physics (boundary layer, cloud microphysics, lack of coupling to the ocean). Determination of the exact causes of error are beyond the scope of this study. Recognizing the deficiencies in the simulated precipitation structure, our goal in subsequent sections is not necessarily to compare specific features in the simulation to specific features in the observed storm at specific times. Instead, we seek to identify and describe basic processes as simulated by the model that aid interpretation of the general structures observed in Bonnie as well as in other storms [e.g., the behavior of reflectivity cores in the eyewall as described by Black et al. (2002)].

## 4. Asymmetric structure

In forthcoming sections, the organization of vertical motion in the eyewall will be shown to result from an interaction of a steady forcing of eyewall asymmetries induced by vertical shear and eyewall mesovortices created through the vorticity dynamics of the eyewall. In this section, we describe persistent eyewall asymmetries

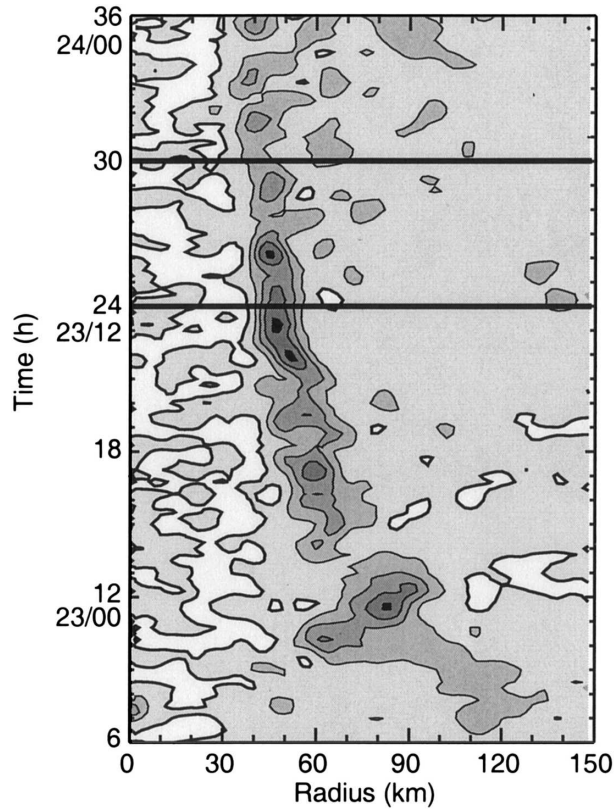


FIG. 7. Time–radius distributions of the azimuthally averaged vertical velocity at 4.5 km. The contour interval is 0.4 m s$^{-1}$ with the zero contour highlighted by the thick solid contour. Horizontal lines bracket the period for which time-averaged quantities are obtained. Dates and times are provided along the vertical axis along with model hour and denoted by date/time (UTC).

by examining the time-averaged vertical motion and precipitation distributions and investigate the mechanisms by which shear produces wavenumber-1 asymmetries in these fields. Time-averaged fields obtained from 3-min model output for the period 24–30 h (valid 1200–1800 UTC 23 August) are examined. To provide context for how this 6-h period relates to the overall evolution of the simulated storm, Fig. 7 shows the radial and temporal distribution of azimuthally averaged vertical motion at 4.8 km. Because of the large radius of maximum wind used for the bogus vortex, in the first several hours after the 2-km grid is initialized, the maximum vertical motion occurs at large radius, but rapidly contracts toward smaller radius. By about 14 h, contraction of the vortex slows and the vertical motion becomes concentrated in the eyewall at a radius of about 60 km. After this time, the eyewall continues a slow contraction, reaching a radius of 40 km by the end of the simulation. Between 14 and 26 h, the azimuthally averaged vertical motion is relatively strong, which con-

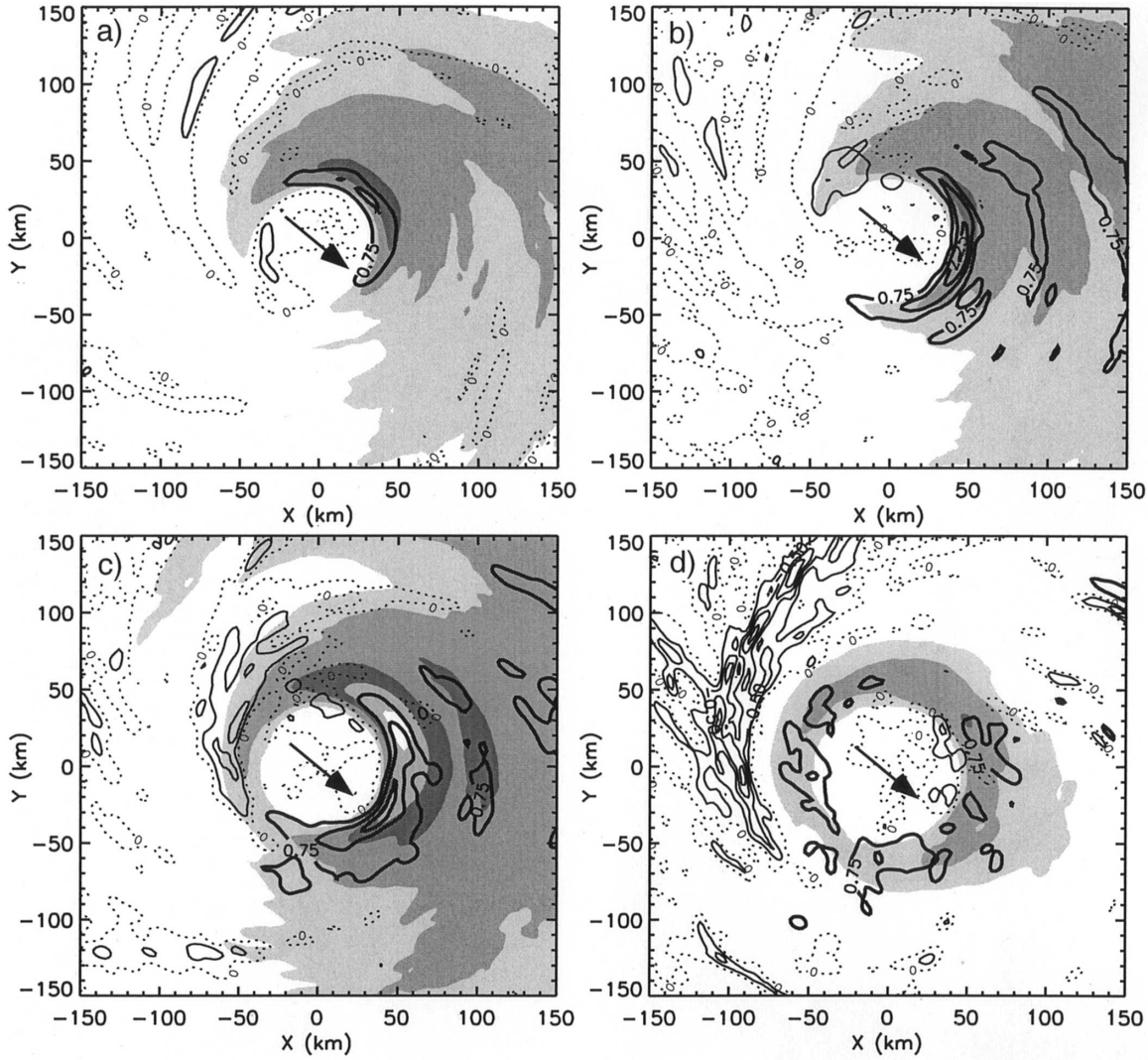


FIG. 8. Time-averaged total precipitation mixing ratio (shading; sum of rain, snow, and graupel) and vertical velocity (contours) for the period between 24 and 30 h (valid 1200–1800 UTC 23 Aug). Precipitation contours are at 0.5, 1, 2, 3, and 4 g kg$^{-1}$. Vertical velocity contours are at intervals of 0.75 m s$^{-1}$ for updrafts (thick solid lines) and 0.25 m s$^{-1}$ for downdrafts (thin solid lines). The zero contour is indicated by dotted lines. Vertical velocity (mixing ratio) fields at (a) 0.9 km (1.1 km), (b) 4.8 km (5.0 km), (c) 7.8 km (8.2 km), and (d) 11.4 km (12.0 km). Vectors indicate the direction of the near-core (70–200-km radius) 850–200-mb shear.

tributes to the gradual intensification of the maximum winds as indicated in Fig. 5b. At about 26.5 h, a final burst of strong convection occurs after which time the mean upward motions, as well as the maximum winds (Fig. 5b), decrease. The period between 24 and 30 h contains some of the strongest vertical motions at 4.8 km and also includes the transition to weaker vertical and tangential circulations, making it a particularly interesting period on which to focus.

Figure 8 shows the 6-h averaged fields of vertical motion and total precipitation mixing ratio at four levels from the top of the boundary layer to the upper troposphere. The shear direction in the outer region (radius 200–800 km, not shown) is west-northwesterly, while in the inner core region (70–200 km), it is northwesterly (see Figs. 9b,d). This inner core shear more directly impacts the asymmetry of the eyewall and is subsequently taken as the direction of the mean shear (e.g., arrows in Fig. 8). The precipitation contours show that the maximum precipitation occurs on the downshear-left (northeastern) side of the storm at all levels. In contrast, the vertical motions show some variation with height. At 0.9 km (Fig. 8a), the maximum upward motion is on the downshear-left side of the storm just inside the region of maximum precipitation. At midlevels (4.8 and 7.8 km; Figs. 8b,c), the maximum upward

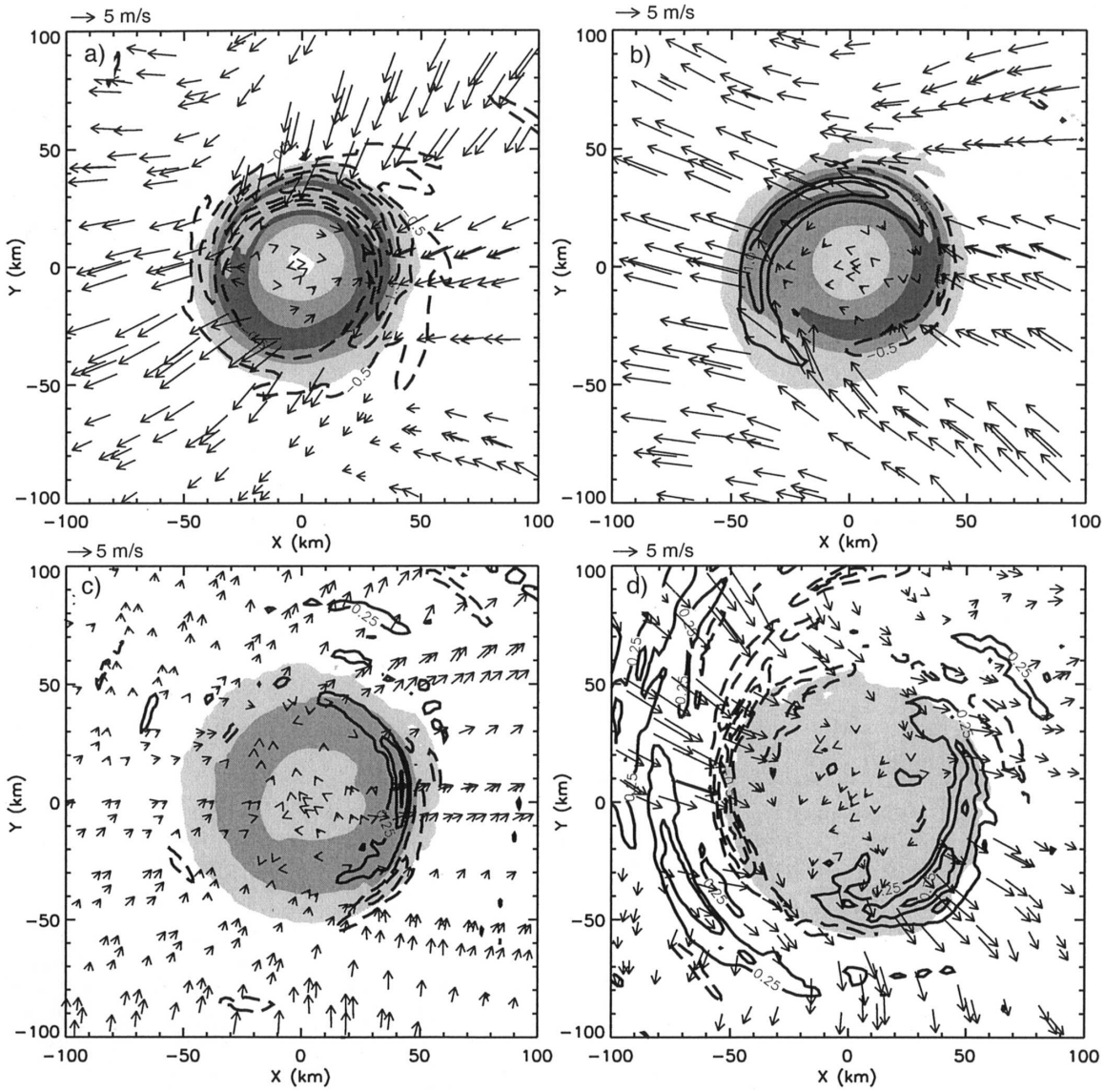


FIG. 9. Time-averaged absolute vertical vorticity (shading), divergence (contours), and asymmetric winds (vectors). Vorticity contours are at 1, 2, 3, and $4 \times 10^{-3}$ s$^{-1}$. Divergence contours are at $0.5 \times 10^{-3}$ s$^{-1}$ intervals, with the zero contour omitted. Positive (negative) values are indicated by solid (dashed) lines. The asymmetric winds are relative to the time-averaged center position at each height. The vector scale is indicated above the upper-left corner. Fields at (a) 0.25, (b) 1.1, (c) 5.0, and (d) 9.9 km.

motions occur on the downshear (southeastern) side of the storm, just upstream (in a cyclonic sense) of the precipitation maximum. At 11.4 km (Fig. 8d), the upward motions are much weaker with the strongest mean ascent on the western and southern sides of the eyewall. Downward motion is strongest at mid-to-upper levels and is concentrated in two areas. The first is on the upshear side of the storm, just downstream of the precipitation maximum and within or just outside of the eyewall. The second is within the eye on the northeastern to eastern side just inside the heavy precipitation associated with the eyewall.

The precipitation and vertical motion distributions are very similar to those observed in Hurricane Norbert (1984) by Marks et al. (1992), in Hurricane Gloria (1985) by Franklin et al. (1993), and in Hurricanes Jimena (1991) and Olivia (1994) by Black et al. (2002). In each case, upward motion typically occurred upstream of the radar reflectivity maximum and downward motion occurred downstream of the reflectivity maximum. Zhu et al. (2004) provided an in-depth description of the downward motion at upper levels on the western side of the eyewall in Bonnie and suggested that it was caused by westerly flow associated with an approaching

shortwave trough impinging on the western side of the storm. They showed that this flow caused convergence and downward motion that acted to suppress convection in the western eyewall.

The suppression of convection on one side of the storm, however, is only a part of the cause of the asymmetry of vertical motion and precipitation. A clear relationship between the storm-relative environmental flow and the asymmetry in vertical motion is seen by overlaying contours of horizontal divergence with contours of vorticity as well as wind vectors associated with the asymmetric wind (determined by subtracting out the azimuthally averaged tangential and radial winds). According to the vorticity balance argument of Willoughby et al. (1984) and Bender (1997), areas of negative (positive) vorticity advection associated with the relative flow should be associated with areas of convergence (divergence). The results (Fig. 9) suggest that this mechanism is at least qualitatively valid since regions with asymmetric inflow (outflow) in the eyewall are associated with convergence (divergence). The relative flow in the boundary layer (Fig. 9a) is from the northeast and the maximum boundary layer convergence occurs on the northeastern side of the eyewall, thereby producing the upward motion maximum there in Fig. 8a. Above the boundary layer, the relative flow is consistent with low-level convergence (Fig. 9b) and upper-level divergence (Fig. 9d) on the downshear side of the storm, with this divergence pattern producing the maximum upward motion on that side of the eyewall at 5 and 8 km (Figs. 8b,c). Interestingly, while the relative flow associated with the shear is readily apparent outside the eyewall at lower and upper levels, the asymmetric flow within the eye is weak and seemingly unrelated to the relative flow. This result suggests that the eyewall acts as an obstacle to the mean flow and behaves much like a containment vessel (McWilliams 1984; McIntyre 1993; Willoughby 1998), in which the eye air remains since the time it was first enclosed within the eyewall, inhibiting ventilation of the eye by the exterior mean flow.

As discussed in the introduction, many studies have described the impact of vertical wind shear on the development of wavenumber-1 asymmetries in the eyewall in terms of the tilt of adiabatic vortices. Vortex tilt impacts vertical motions in adiabatic vortices in two ways: 1) the tilting induces temperature asymmetries as required for the flow to remain balanced (Jones 1995; Wang and Holland 1996a), with these temperature asymmetries being produced by rising or sinking of dry air; and 2) the subsequent development of upward motion 90° to the right of the tilt direction as a result of the interaction of the vortex flow with the temperature asymmetries generated by 1) (Jones 1995; Wang and Holland 1996a; Frank and Ritchie 1999).

To investigate the effects of shear-induced vortex tilt, the center position at 8 km was determined at each time following the method outlined in section 3; that is, the centroid of the pressure field was estimated by minimizing its asymmetry. The displacement between the centers at the surface and 8 km was then used as a proxy for vortex tilt. Figure 10 shows the azimuthal distributions of the radially averaged (30–60 km) wavenumber-1 upward motion and potential temperature at 4.8 and 5.0 km, respectively, as well as the tilt azimuth as a function of time for the period 18–36 h (0600 UTC 23 August to 0000 UTC 24 August). The vertical motion and temperature asymmetries are determined with respect to the center location at 5 km. Given the relatively coarse temporal resolution for this period (15 min) and the discrete nature of the center locations (movement in increments of the grid spacing of 2 km), some temporal smoothing has been applied to the results presented in Fig. 10 (as well as Fig. 11). The initial 12 h on the 2-km grid are not shown since this period is strongly influenced by the adjustment of the model to the high-resolution grids (Fig. 7). As indicated in Fig. 10, the maximum wavenumber-1 upward motion occurs on the east-southeastern side of the storm, slightly to the left of the shear vector, is coincident with a cold anomaly, and is clearly occurring in the direction of tilt. Variations in the tilt of the vortex are generally aligned with variations in the axis of peak wavenumber-1 upward motion and cold potential temperatures, implying a strong linkage between vortex tilt and vertical motion asymmetries. These results are similar to those of Rogers et al. (2003) and Zhu et al. (2004), who also showed that the maximum wavenumber-1 upward motion occurs in the downtilt direction.

Frank and Ritchie (1999), using idealized simulations at 15-km horizontal resolution, found that during early stages after shear was imposed the precipitation was dominated by the convective parameterization and the maximum upward motion was located downshear-right, consistent with Jones (1995). Once grid points in the eyewall reached saturation and the precipitation was dominated by the explicit microphysical parameterization, the maximum upward motion shifted to the downshear-left side. They suggested that grid-scale latent heating eliminated the downtilt temperature anomaly so that the Jones mechanism could not occur. In the Bonnie simulation, however, temperature anomalies consistent with the tilt do form. Two explanations may account for the cold anomaly despite the latent heating. First, thermodynamic budgets derived from a simulation of Hurricane Andrew (1992) by Zhang et al. (2002)

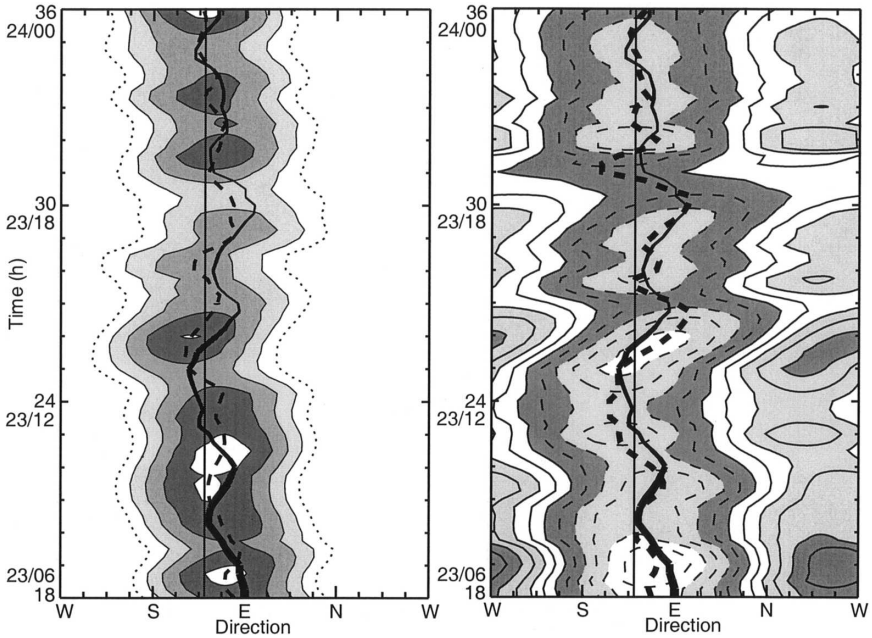


FIG. 10. Time–azimuth distributions of wavenumber-1 (a) vertical motion at 4.8 km and (b) potential temperature at 5.0 km averaged between radii of 30 and 60 km. In (a), updraft contours are drawn at an interval of 0.25 m $s^{-1}$ with the zero contour indicated by the dotted line. The dashed line shows the axis of peak wavenumber-1 upward motion. In (b), the contour interval is 0.3 K with positive (negative) values indicated by solid (dashed) lines. The thick dashed line shows the axis of the cold temperature anomaly. The solid curves in (a) and (b) show the direction of vortex tilt, with the thickness of the line proportional to vortex tilt (thicker for larger tilt). The solid vertical line indicates the direction of the near-core 850–200-mb shear vector. Dates and times are provided along the vertical axis along with model hour and denoted by date/time (UTC).

suggest that adiabatic cooling in eyewall updrafts may slightly exceed the latent heating so that some cooling occurs in the eyewall. Second, even if the latent heating exactly balances the adiabatic cooling, a cold anomaly can arise through differential warming associated with adiabatic warming of dry, subsiding air on the uptilt side. In either case, it appears that the interaction of the mean vortex flow with these temperature anomalies produces weaker forcing for vertical motion than the more direct effects of the storm-relative flow or vortex tilt.

The variation of the storm tilt with time is shown in Fig. 11. The rapid increase in shear during the early stages produces a tilt of ~12 km by 18 h that is then gradually reduced by half by 26.5 h as the upper center moves through two cyclonic loops. During the period of larger tilt, the wavenumber-1 upward motion is strongest (Fig. 10a). After 26.5 h, the tilt remains relatively small as the storm center at 8 km continues to loop in a generally cyclonic fashion downshear and slightly to the left of the shear vector. The occurrence of a damped looping motion of the upper center supports the hypothesis of Reasor et al. (2004) that the mechanism by which hurricane vortices resist tilting by vertical wind shear is governed by the dry adiabatic dynamics and enhanced by the moist physics. Reasor et al. (2004) showed that realignment occurs through projection of the tilt asymmetry onto two types of vortex Rossby waves: a quasi mode, or near-discrete, vortex Rossby wave and sheared vortex Rossby waves. The quasi-mode is characterized by long-lived precession of the upper part of the tilted vortex relative to the lower part. Initially, the upper vortex is tilted downshear. Subsequently, upward projection of the circulation associated with the low-level vortex causes anticyclonic precession of the upper vortex upshear and eventual realignment, followed by additional cycles of tilting, precession, and realignment. The damping rate of the quasi mode depends on the characteristics of the vortex, specifically the radial gradient of the potential vorticity (PV) at a critical radius where the precession frequency equals the angular rotation rate of the mean flow. A negative radial PV gradient at the critical radius produces damping, and the stronger the gradient, the faster the damp-

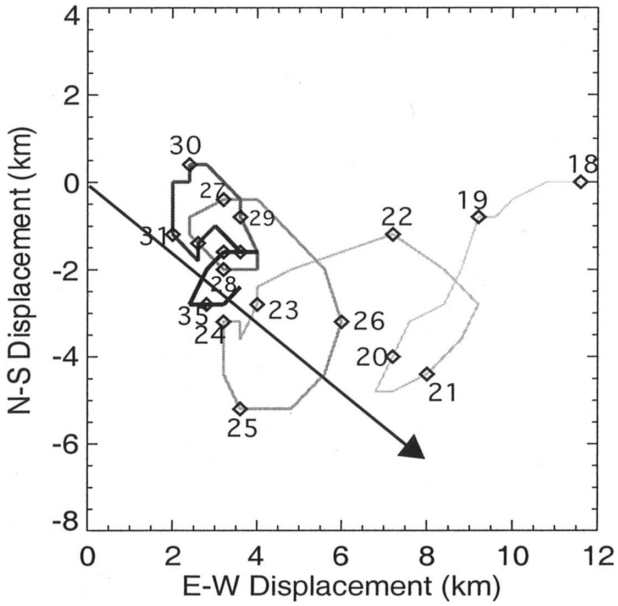


FIG. 11. Displacement of the storm center at 8 km from the surface center. Time (model hour) is indicated by the numbers while the line gets darker with time. The arrow indicates the direction of the near-core 850–200-mb shear vector.

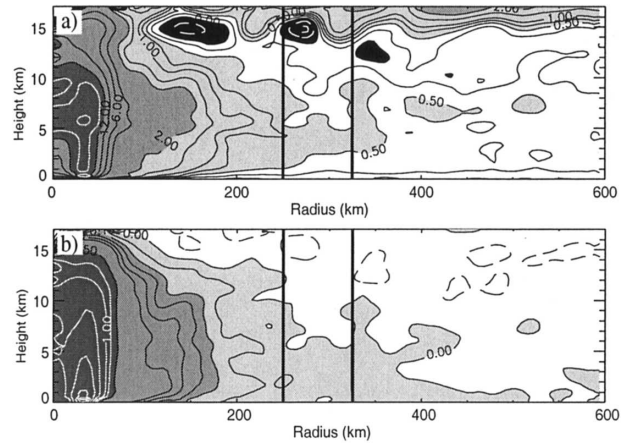


FIG. 12. Vertical cross sections of the time- and azimuthally averaged (24–25 h) (a) potential vorticity and (b) relative vorticity obtained from the 6-km grid. Contours for PV are drawn at −1, −0.5, 0, 0.25, 0.5, 0.75, 1, 1.5, 2, 4, 6, 9, 12, 15, and 20 PV units ($10^{-6}$ m$^2$ s$^{-1}$ K kg$^{-1}$). Negative values are indicated by black shading, positive values by increasingly darker gray shades at 0.5, 2, and 12 PV units. Contours of relative vorticity are at −0.1, −0.05, 0, 0.05, 0.1, 0.15, 0.2, 0.25, 0.5, 0.75, 1, 1.5, 2, and $2.5 \times 10^{-3}$ s$^{-1}$. Negative values are indicated by white, positive values by increasingly darker gray shades at 0, 0.1, and $0.5 \times 10^{-3}$ s$^{-1}$. Solid straight lines indicate the range of estimated radii where the value of the precession frequency equals the density-weighted, vertically integrated angular velocity.

ing of the precession. With stronger damping, the vortex achieves a downshear-left equilibrium tilt, while in the limit of no damping, indefinite tilting, precession, and realignment occurs. A positive radial PV gradient leads to a tilt instability [exponentially growing tilt; see Reasor et al. (2004)] in which the upper and lower vortices continually move apart.

To illustrate that the damping of the precession (Fig. 11) is consistent with the radial PV gradient, Fig. 12 shows vertical cross sections of the azimuthally and time-averaged (24–25 h) PV and relative vorticity. Superposed on these fields are estimates of the minimum and maximum values of the critical radius where $V/r \sim \omega = 2\pi/T_p$, $V$ is the azimuthally averaged tangential wind, $r$ is radius, $\omega$ is the precession frequency, and $T_p$ is the time required for the center at 8 km to complete one of the loops shown in Fig. 11 (estimated to be between 3 and 5 h). Since the theoretical work of Reasor et al. (2004) is based upon a barotropic vortex, here we estimate the critical radius using a radial profile of the density-weighted, vertically integrated angular velocity. We use $T_p = 3$ and 5 h to get the vertical lines in Fig. 12. From Fig. 12a, the critical radius is seen to lie in a region where PV is generally decreasing slowly with radius so that, at least in the context of the theory for an adiabatic vortex, the results are consistent with a damped precession. Moist processes likely accelerate the damping (Reasor et al. 2004) so that the vortex tilt is rapidly reduced between 18 and 27 h (Fig. 11). The vorticity profile (Fig. 12b) is characterized by a negative radial gradient with negative relative vorticity developing at low levels between 400 and 500 km (~10 times the radius of maximum winds) and a possible change in the sign of the gradient further out. This vorticity profile differs from that of Jones (1995) in which the relative vorticity is negative near a radius of 200 km (twice the assumed radius of maximum wind) and the radial gradient of vorticity changes sign near 250 km. Reasor et al. (2004) argue that the critical radius in the Jones (1995) case lies within the region of positive PV gradient so that the Jones profile is associated with a growing tilt asymmetry. Figure 12 suggests that a critical radius within the negative PV gradient region may be more realistic than one within a positive PV gradient region.

Key differences between the simulation results in Fig. 11 and the results of Reasor et al. (2004) are that in the Bonnie simulation, the looping motion of the upper center relative to the lower center is much smaller (confined to the downshear direction as opposed to the entire downshear-left semicircle) and the equilibrium tilt is only slightly left of shear while Reasor et al. obtain an equilibrium tilt 90° to the left of the shear vector. Interestingly, Wu et al. (2006) describe a simulation of Hurricane Erin (2001) in which the tilt direction and upward component of the wavenumber-1 asymmetry

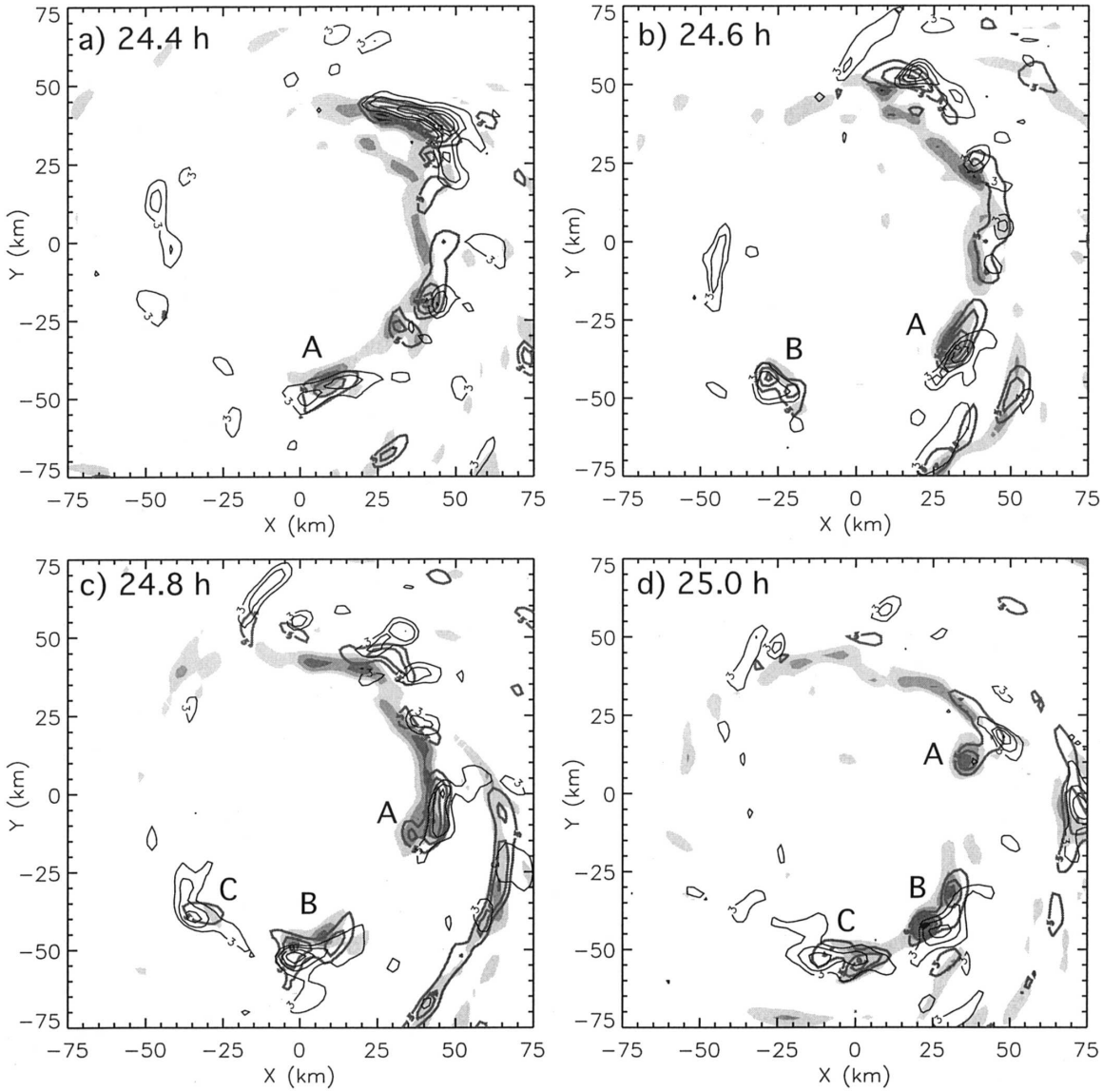


FIG. 13. (a)–(h) Vertical velocity at 1.7, 4.8, and 7.8 km MSL. Shading shows updrafts at 1.7 km at contour levels of 1.5, 3, 4.5, and 6 m $s^{-1}$. Thick contours show updrafts at 4.8 km while thin contours show updrafts at 7.8 km at values of 3, 6, 9, and 12 m $s^{-1}$. The time corresponding to each panel is shown in the upper-left corner. Letters indicate updrafts discussed in the text. The dashed line in (g) indicates the location of the remnant of the organized rainband in (f).

varied from 60° to the left of the shear on 9 September to 90° on 10 September. The common factor in the Bonnie and Erin simulations is that the mean tilt direction and direction of the convective asymmetry are generally in the direction of the low-level storm-relative inflow (Figs. 9–11 herein and Fig. 16 of Wu et al. 2006), which is where low-level convergence in the eyewall is maximum. In the Bonnie case, the low-level inflow is on the downshear side of the eyewall while in the Erin case, the low-level inflow is ~45–60° to the left of downshear on 9 September and ~90° to the left on 10 September. These results imply that the convection is anchored to the side of the eyewall where the low-level inflow and convergence is occurring. Because the vortex tilt and the upward motion asymmetry are inextricably linked, the tilt cannot depart far from the inflow side of the storm. Consequently, instead of the larger looping motion to the left of the shear direction seen in the adiabatic model of Reasor et al. (2004), the looping motion and the equilibrium tilt in the full-physics cases are confined to the inflow side of the storm. The angle between the directions of the low-level inflow and the

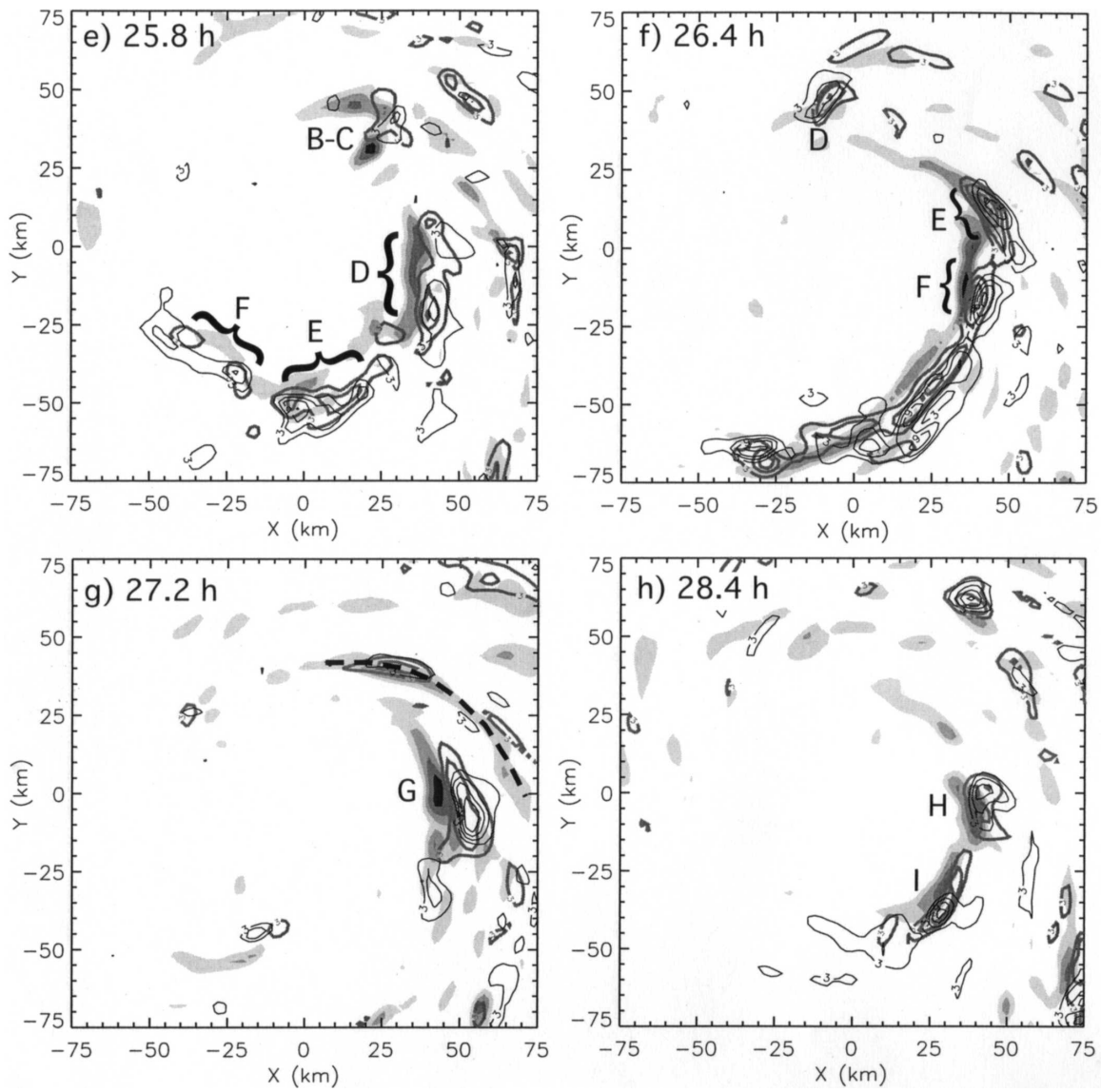


FIG. 13. (*Continued*)

vertical shear is likely related to the shape of the profile of the environmental winds [e.g., a unidirectional shear profile versus a curved shear profile, in the sense of hodographs as described by Weisman and Klemp (1986)]. Idealized simulations employing more complex vertical shear profiles (i.e., other than unidirectional) are needed to describe more clearly the relationships between vertical shear, relative flow, vortex tilt, and convective asymmetries.

## 5. Convective updrafts and eyewall mesovortices

Although the time-averaged vertical motion fields show a relatively smoothly varying asymmetric vertical motion pattern, the upward motion in the eyewall at any instant in time is typically comprised of a small number of convective updrafts that occupy only a relatively small percentage of the eyewall area (Jorgensen et al. 1985; Black et al. 1996; Braun 2002; Eastin 2003). In this section, the structure of these updrafts is investigated in much greater detail with emphasis on their formation, vertical structure, and evolution.

### *a. Updraft structure*

The vertical structure of the updrafts at several different times are indicated in Fig. 13, which overlays contours of upward motion at 1.7, 4.8, and 7.8 km. The updrafts at each level are easily tracked using the 3-min

model output and the contoured updrafts are frequently found to be vertically coherent structures that move cyclonically around the eyewall. At some times, the updraft structures are single, well-defined updrafts, at other times they are small clusters of updrafts. The first five panels of Fig. 13 track the evolution of three updrafts or updraft clusters labeled A, B, and C. At 24.4 h (Fig. 13a), a continuous band of weak upward motion with several embedded local maxima extends around the eastern half of the storm at low levels, with the more intense cells associated with more isolated updrafts at mid and upper levels. Updraft A, on the southern side of the eyewall, extends vertically throughout the troposphere. Twelve minutes later (Fig. 13b), updraft A has rotated cyclonically about the center and remains nearly vertically aligned. Updraft B has formed on the south-southwest side of the eyewall, extends into the upper troposphere, and possesses two updraft cores at midlevels. After another 12 min (Fig. 13c), updraft A has moved to the eastern side of the eyewall, updraft B is more clearly a cluster of two adjacent deep updrafts, and updraft C has formed with strong vertical motions ($>9$ m s$^{-1}$) extending through the 8-km level. By 25 h (12 min later), updraft A has begun to weaken on the northeastern side of the eyewall, while updrafts B and C both exhibit double updraft structures and are gradually getting closer together. By 25.8 h (Fig. 13d), updrafts B and C have merged and are now dissipating on the northeastern side of the eyewall. New updraft clusters have formed on the eastern and southern sides of the storm (D, E, and F[3]) with the latter two eventually merging with subsequent updrafts (Fig. 13e) to form a well-defined and nearly continuous rainband by 26.4 h (Fig. 13f). This rainband represents the last burst of convection seen in Fig. 10a, and immediately precedes the time at which the vortex becomes nearly vertically realigned (Fig. 11), stops intensifying (Fig. 5b), and transitions to a period of weaker vertical motion (Fig. 7b) with fewer, more isolated convective updrafts (Figs. 13g,h). At 27.2 h (Fig. 13g), a single deep updraft has formed on the eastern side of the eyewall in the wake of the more organized rainband (dashed line). At the last time shown (Fig. 13h), two vertically coherent updraft structures (H, I) are seen on the southeastern side of the eyewall.

In general, the updrafts, or updraft clusters, are observed to form on the southern (downtilt right) side and to dissipate on the northern (downtilt left) side, similar to the conceptual model of Heymsfield et al. (2001).

[3] At this time (Fig. 13e), updraft cluster F is just forming, but is still poorly defined. Subsequent times (not shown) reveal it to be a more distinct feature.

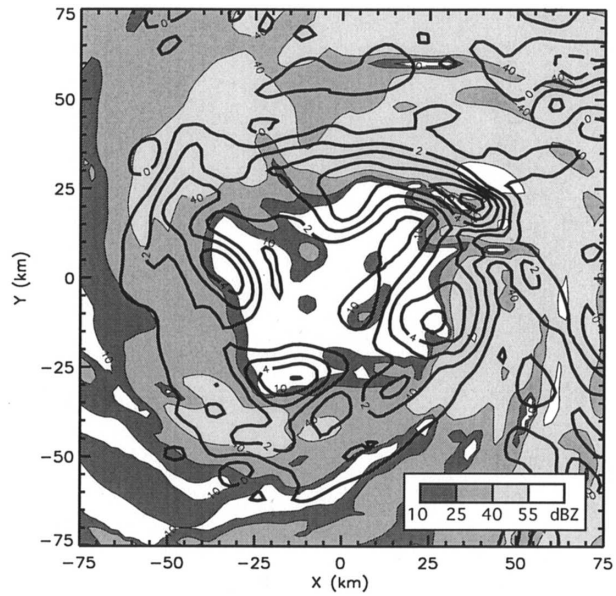


FIG. 14. Simulated radar reflectivity (shading) and absolute vorticity at 25.8 h (corresponding to Fig. 13e) and 1 km MSL. The contour interval for vorticity is $1 \times 10^{-3}$ s$^{-1}$.

However, in contrast to their conceptual model, the updrafts are not starting off shallow on the southern side and growing to maximum height on the northern side, but are instead seen to extend through the depth of the troposphere virtually from their inception. Although the updrafts are deep shortly after forming on the southern side, the updrafts reach maximum intensity on the east-southeastern (downtilt) side of the eyewall while precipitation growth peaks on the northeastern (downtilt left) side, as indicated in the time–mean fields in Fig. 8. Relative to the scale of the vortex, the updrafts are nearly vertically aligned updraft towers with a small outward and azimuthally upstream tilt. Of course, when viewed on the scale of the updrafts, they exhibit substantial tilt, as is common in hurricanes (Jorgensen 1984; Black et al. 1996).

### b. *Vorticity dynamics of the updrafts*

The mechanisms that control the timing and location of the updrafts are associated with mesoscale vortices in the eyewall. In Fig. 14, the absolute vorticity is overlaid on the simulated radar reflectivity and it can be seen that mesovortices generally occur along the inner edge of the eyewall reflectivity area. Also apparent is the polygonal shape of the eyewall, in this case forming a pattern somewhere between a square and pentagon in the reflectivity field. Polygonal eyewalls have been observed by Lewis and Hawkins (1982) to be a frequent occurrence in strong hurricanes. Schubert et al. (1999)

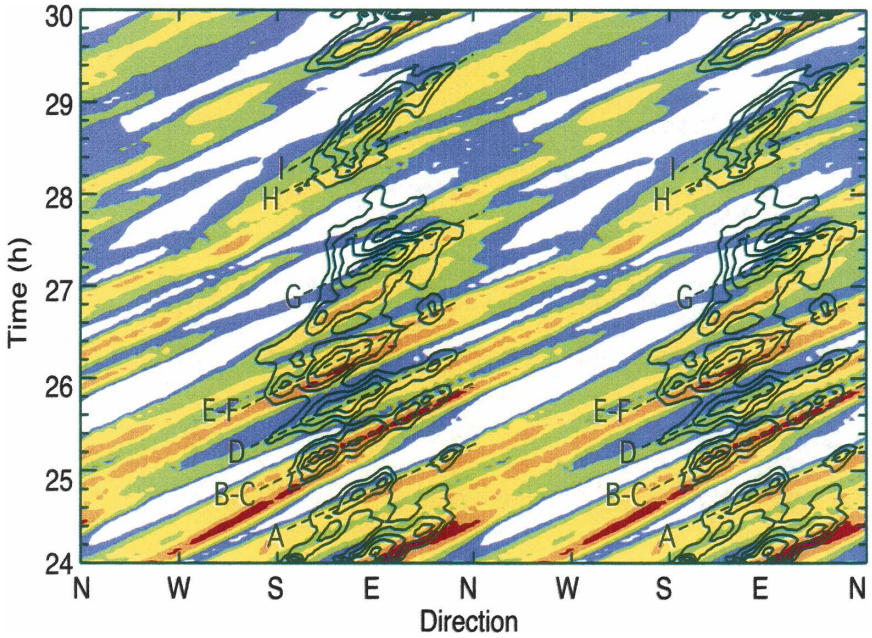


FIG. 15. Time–azimuth distributions of radially averaged (30–60 km) absolute vorticity (colors, contour interval of $0.25 \times 10^{-3}$ s$^{-1}$ starting at $1.5 \times 10^{-3}$ s$^{-1}$) and vertical velocity (contours, 0.2 m s$^{-1}$ intervals starting at 0.8 m s$^{-1}$) for the 1–4-km layer. The plot has been extended to two revolutions around the center. Dashed lines and letters identify the individual updrafts or updraft clusters shown in Fig. 13.

and Kossin and Schubert (2001) showed using idealized simulations that polygonal eyewalls form as a result of the vorticity dynamics of the eyewall region. An axisymmetric annulus of potential vorticity, representative of the distribution of vorticity within the eyewall of a hurricane, satisfies the Charney–Stern condition for inflection-point (mixed barotropic/baroclinic) instability (Montgomery and Shapiro 1995; Ren 1999; Nolan and Montgomery 2002). In the limiting case of a barotropic vortex, this corresponds to Rayleigh's inflection point theorem (Drazin and Reid 1981). In the case of an unstable basic state, small perturbations typically grow rapidly to form polygonal eyewalls and mesovortices. Depending on the initial characteristics of the annulus of vorticity, the mesovortices may mix into the center and coalesce to form a vortex monopole (Schubert et al. 1999; Kossin and Schubert 2001) or they may form a set of long-lived mesovortices whose number may vary (Kossin and Schubert 2001; Montgomery et al. 2002). Kossin and Schubert (2001) found that monopoles are more likely to form from smaller or radially broader initial vorticity annuli, while stable mesovortices are more likely to form from larger and radially thinner vorticity annuli. The relatively large radius of Bonnie in the simulation (~40–50 km compared to the observed 30–40 km) apparently favors the development of the mesovortices.

To demonstrate how eyewall updrafts are related to the mesovortices, we consider the distributions of absolute vorticity and vertical motion determined from density-weighted mean values between heights of 1 and 4 km. The mean values are used instead of values from a single height to accentuate the deeper updraft structures and minimize the impact of shallow updrafts that occur near the top of the boundary layer. The mesovortices often extend up to the 5-km level or above so that they are vertically coherent structures that are well represented in the layer averages. Figure 15 shows a Hovmöller diagram of the radially averaged (30–60 km) vorticity and vertical velocity for the 1–4-km layer. The vorticity field shows positive vorticity anomalies that rotate around the storm at least once and, in some cases, several times. When these positive vorticity anomalies move into the southern to southeastern parts of the eyewall, updrafts form coincident with or immediately trailing the vorticity anomalies in time in a given direction. Each of the updrafts discussed in Fig. 13 are indicated in Fig. 15 with updrafts B–C and E–F sufficiently close together that they appear as a single updraft. Each of the updrafts is preceded by a mesovortex that has moved around the western side of the eyewall, with some mesovortices initiating more than one round of convection. In addition, each updraft tends to enhance the vorticity by vortex compression associated

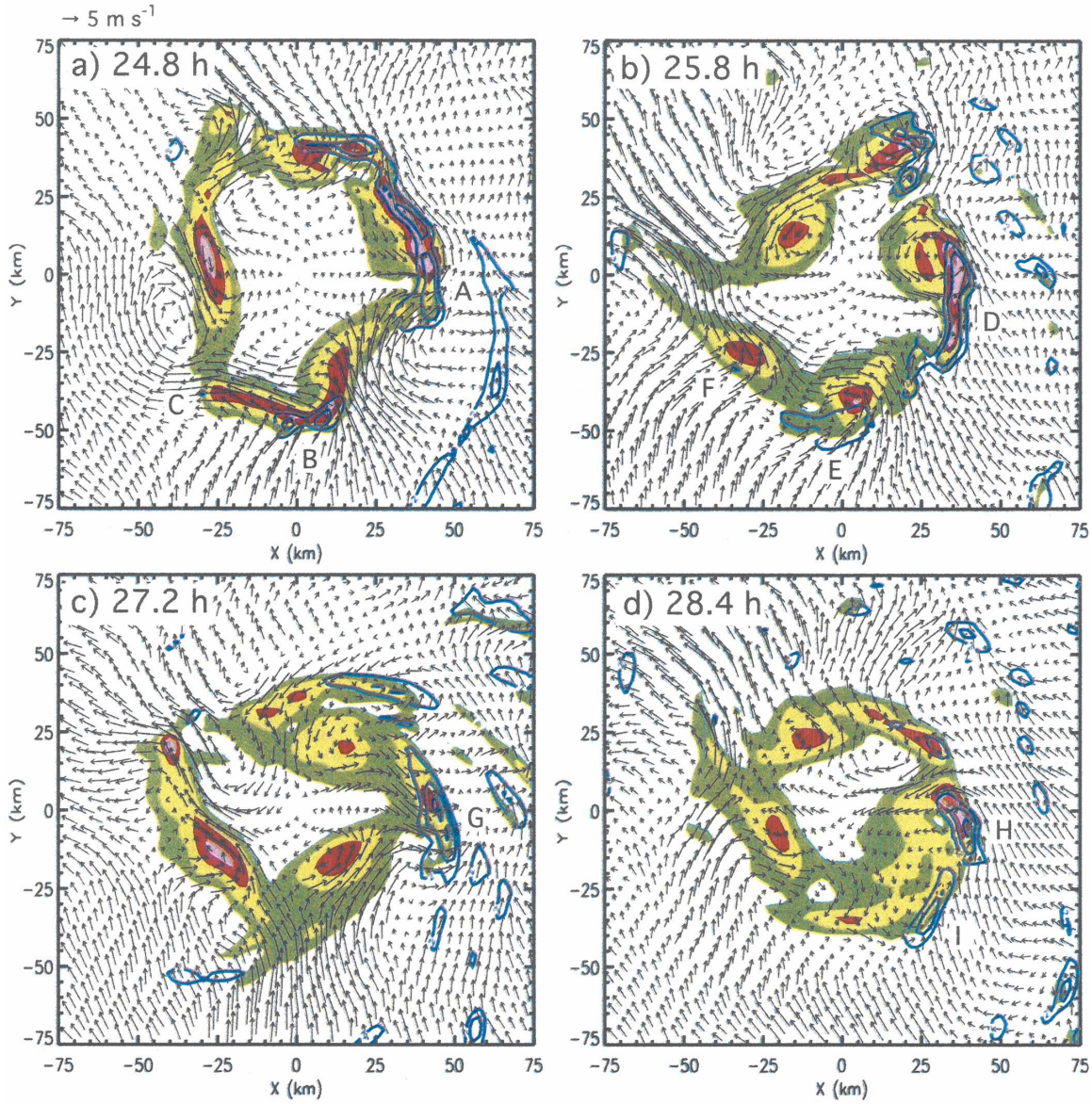


FIG. 16. (a)–(d) Absolute vorticity (colors), vertical velocity (contours, updrafts only), and storm-relative asymmetric wind vectors averaged over the 1–4-km layer at the times indicated in the upper-left corner of each panel and corresponding to Figs. 13c,e,g,h. The contour interval for vorticity is $1 \times 10^{-3}$ s$^{-1}$ starting at $2 \times 10^{-3}$ s$^{-1}$. Contours of vertical motion are at 2 m s$^{-1}$ intervals starting at 2 m s$^{-1}$. Asymmetric wind vectors are obtained by subtracting the azimuthally averaged radial and tangential winds. The vector scale is indicated above the upper-left corner of (a).

with low-level convergence (e.g., Fig. 17a), which helps to intensify the mesovortices or generate new mesovortices, and, in general, maintain the annulus of vorticity associated with the eyewall. As an example, consider the mesovortex that triggers updraft B–C in Fig. 15. It starts on the northwestern side of the storm and initiates updrafts B and C when it moves to the southern side of the eyewall. Its vorticity is modified or enhanced by the updraft and subsequently rotates around the storm again to initiate updraft G. A similar evolution can be seen for the mesovortex that initiates updraft E–F and subsequently updrafts H and I.

A more detailed view of the relationship between these mesovortices and eyewall updrafts is provided in Fig. 16, which shows the distributions of vorticity, vertical motion, and asymmetric winds for the 1–4-km layer for the times corresponding to Figs. 13c,e,g,h. Several key findings are apparent. Each deep updraft structure is generally associated with a mesovortex. Noting that the mesovortices move cyclonically around the

eyewall, in cases where the mesovortex has a closed cyclonic circulation, it produces relative outflow (inflow) on its trailing (leading) sides. Where the outflow associated with the mesovortex meets with the general area of southeasterly inflow (see also Fig. 9b), there is enhanced convergence (cf. Figs. 16b and 17a, updrafts D and E) and in the area of vortex-induced inflow, there is reduced convergence or divergence. As a result, the enhanced convergence trailing the mesovortex leads to the formation of the updraft there.

In other cases (e.g., updrafts B and F), updrafts form along mesovortices that do not have a closed cyclonic circulation, but instead are associated with enhanced (reduced) tangential flow radially outside (inside) of the mesovortex. The notion that intense vortices provide a protected environment within their cores is now a familiar one in geophysical fluid dynamics (McWilliams 1984; McIntyre 1989; Carnevale et al. 1992; McIntyre 1993; McWilliams et al. 2003). We can apply these ideas to the eyewall mesovortex problem. Accordingly, the mesovortices act as obstacles to the inflowing air, with the stiffest resistance residing where the local potential vorticity gradient (the Rossby restoring mechanism for vortex deformations) is maximum. In many of the cases shown here, the updraft forms radially outside of the mesovortex core, but as the updraft intensifies the vorticity by vortex tube stretching, a closed cyclonic circulation develops, and the updraft shifts to the trailing side of the mesovortex (e.g., B–C in Figs. 13e and 16b). These results indicate a greater complexity in the relationship between vertical motion and vorticity than expectations from simple Ekman pumping considerations in which the updraft at the top of the boundary layer would be collocated with the mesovortex (Chen and Yau 2001; Fulton 2001).

The time-averaged asymmetric flow (Fig. 9) suggests that the eyewall should act as a barrier to the environmental relative flow, just as the mesovortices impede the horizontal asymmetric flow of the eyewall region. The air–mass exchange problem on the system (vortex) scale is more complex, however, because the potential vorticity distribution of a mature hurricane is typically not monotonic with radius. As discussed above, the ringlike PV structure of the eyewall renders it susceptible to internal instabilities (polygonal eyewalls and mesovortices) that act to turn the eye/eyewall region inside out. Indeed, Fig. 16 suggests that much of the exchange between eye air and environmental air outside the eyewall occurs in association with the eyewall mesovortices (Schubert et al. 1999; Kossin and Schubert 2001; Persing and Montgomery 2003; Eastin 2003).

Together, these results suggest a strong linkage between eyewall mesovortices, the relative flow associated with the environmental shear, and the convective updrafts in the eyewall. Updrafts form when the mesovortices move into the region where the relative flow supports the upward component of the wavenumber-1 asymmetry in vertical motions. At the same time, the low-level convergence associated with the updrafts modifies the vorticity field so as to maintain or intensify the annulus of potential vorticity and occasionally generate new mesovortices.

### c. *Quantitative aspects of eyewall mesovortices and related updrafts*

The idealized simulations of Kossin and Schubert (2001) produced strong local pressure perturbations. They defined the pressure perturbation as being the difference between the local pressure and that at a radius of 100 km. From their Figs. 4 and 6, perturbations from the azimuthal mean can be roughly estimated as ~5–15 hPa, and perhaps stronger in their experiments 4–7, for which pressure fields were not shown, but final pressures falls were quite large. The magnitude of these perturbations is fairly large. Marks and Black (1990) and Black and Marks (1991) described observations taken during a reconnaissance flight through a very strong mesovortex in the eyewall of Hurricane Hugo (1989). This mesovortex was clearly defined even in the total wind field (as opposed to just in the asymmetric flow) and was associated with a surface pressure approximately 7 hPa lower than the mean value in the eye and 12 hPa lower than a linear profile across the eyewall. Pressure perturbations from the simulation of Bonnie are shown for 25.8 h in Fig. 17b and are derived from the density-weighted mean values for the 1–4-km layer by removing the azimuthal mean pressure field. Relative minima in the perturbation pressure field are associated with each of the mesovortices in the eyewall and have maximum amplitude of about 1.5 hPa at this time and up to 3 hPa at other times. The larger pressure perturbations in the Kossin and Schubert (2001) simulations are likely related to the amplitude of the azimuthally averaged vorticity used to initialize their simulations. They showed that the larger the initial vorticity of the annulus, the larger the final pressure fall. They used vorticity annuli with amplitudes ranging from 22.5–44.8 $\times 10^{-3}$ s$^{-1}$ whereas the simulation of Bonnie produces maximum vorticity values of about 14 $\times 10^{-3}$ s$^{-1}$ and azimuthally averaged values up to 5 $\times 10^{-3}$ s$^{-1}$.

Marks and Black (1990) and Black and Marks (1991) estimated wind speed perturbations associated with the mesovortex in Hugo to be 20–30 m s$^{-1}$ compared to local maximum wind speeds of 90 m s$^{-1}$ and azimuthally averaged winds likely considerably lower. Fulton (2001), in an analysis of the high resolution simulation

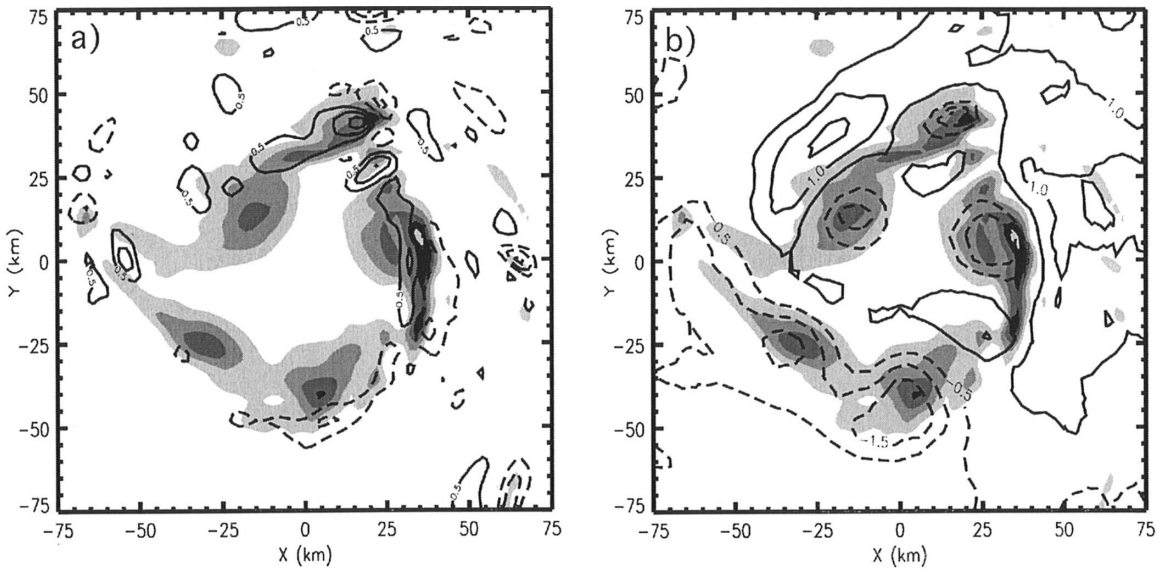


FIG. 17. (a) Absolute vorticity (shading) and divergence (contours) at 25.8 h averaged over the 1–4-km layer. Contour intervals for vorticity and divergence are $1 \times 10^{-3}$ s$^{-1}$ with vorticity starting at $2 \times 10^{-3}$ s$^{-1}$. (b) Absolute vorticity (shading) and pressure perturbation (contours) for the same time and layer. Pressure perturbation is obtained by subtracting the azimuthal mean pressure. The contour interval is 0.5 hPa. In (a) and (b), positive (negative) values are indicated by solid (dashed) lines and the zero contour is omitted.

of Hurricane Bob (1991) by Braun (2002), found that the maximum tangential winds were consistently 20%–30% higher than the azimuthal mean values. Montgomery et al. (2002) showed using laboratory water tank experiments that long-lived mesovortices can produce winds 50% greater than the parent vortex. Wind speed perturbations associated with the mesovortices in Fig. 16 reach up to 10–15 m s$^{-1}$, so that peak winds (azimuthal mean plus anomalies) at the top of the boundary layer are up to 20%–30% larger than the azimuthally averaged values at the same level, consistent with the abovementioned studies.

This pattern of updraft development associated with mesovortices is strikingly similar to the tracking of convective cores in hurricanes Jimena (1991) and Olivia (1994) as described by Black et al. (2002). They tracked the positions of reflectivity cores in the eyewalls of these two hurricanes and found a tendency for cell formation to occur on the downshear side and cell dissipation to occur on the upshear side of the eyewall, consistent with the maximum precipitation occurring in the downshear-left portion of the eyewall. Furthermore, they noted that clusters of longer-lived cells could be clearly tracked for several orbits around the eyewall, with older cells in the clusters dissipating on the upshear side and newer cells forming on the downshear side. Such behavior is consistent with the presence of long-lived mesovortices as depicted in Fig. 15.

The individual cells and clusters of cells observed by Black et al. (2002) tended to move more slowly than the mean winds in the eyewall, with orbital velocities generally between 56% and 72% of the mean flow at the radius of maximum wind. The orbital velocity of the mesovortices in the simulation, estimated from Fig. 15, is approximately 37 m s$^{-1}$ or about 70% of the azimuthal mean flow. The movement of the mesovortices at a speed slower than the mean flow is consistent with simple expectations for vortex Rossby waves (Montgomery and Kallenbach 1997; Chen and Yau 2001; Fulton 2001).

## 6. Conclusions

In agreement with observations (Jorgensen et al. 1985; Black et al. 1996; Eastin 2003) and previous simulations (Braun 2002), eyewall upward motions are found to be associated with small-scale convective updrafts. Occasionally, the updrafts occur in sufficient number and proximity that they merge together to form organized rainbands. The updrafts form, intensify, and dissipate on the downtilt-right, downtilt, and downtilt-left sides of the eyewall, respectively. Consequently, when averaged in time, the vertical motion field exhibits a pronounced wavenumber-1 asymmetry with peak upward motion on the downtilt (eastern to southeastern) side.

Many mechanisms for generating asymmetry as a result of vertical wind shear have been described in the literature. One such mechanism (Willoughby et al. 1984; Bender 1997; Frank and Ritchie 2001) requires

that storm-relative asymmetric inflow (outflow) in the eyewall generates convergence (divergence) as a result of a quasi-balance between horizontal vorticity advection by the relative flow and vortex stretching or compression. The vertical motion field is then determined by the vertical distribution of this divergence field. In the present case, the relative asymmetric flow varies with height such that inflow and convergence occur on the northeastern (downshear left) side of the eyewall within the boundary layer, on the southeastern (downshear) side in the lower troposphere above the boundary layer, and on the northwestern (upshear) side in the upper troposphere. Outflow and divergence occur on the opposite sides in each layer. The convergence within the boundary layer on the northeastern side produces maximum upward motion on that side at the top of the boundary layer. However, above the boundary layer, the low-level convergence and upper-level divergence on the southeastern side promote deep upward motion there while low-level divergence and upper-level convergence promote downward motion on the northwest side.

The vertical motion asymmetry is also consistent with the mechanisms related to the tilt of the vortex. The mean tilt of the vortex is just to the left of the shear vector and is in the same direction as the midlevel upward motion and a cold potential temperature anomaly, in agreement with expectations for a balanced vortex (Jones 1995). Although the interaction of the mean tangential flow with the temperature anomaly field might be expected to shift the upward motion to the right of the tilt direction (Jones 1995), the upward motion remains locked in the downtilt direction, presumably because the effects of the relative flow and vortex tilt are the dominant forcing for the vertical motion asymmetry. Temporal variations of the tilt are consistent with the recent findings of Reasor et al. (2004). They showed that the tilt of an adiabatic vortex resulting from vertical wind shear can be projected onto two modes of vortex Rossby waves, sheared waves and a quasi mode. The latter is associated with precession of the upper vortex relative to the lower vortex such that vertical alignment is maintained. In the simulation of Bonnie, a 12-km tilt at 18 h is gradually reduced to 3–4 km by 27 h as the upper center undergoes two cyclonic loops (precession cycles). Thereafter, the tilt remains small as the upper center continues its precession in smaller cyclonic loops. Variations in the direction of the axes of wavenumber 1 upward motion and cold temperature anomaly coincide with variations of the tilt direction associated with the precessing upper vortex. The wavenumber-1 upward motion peak is strongest during the two larger precession loops, and then diminishes for the remainder the simulation as the tilt remains small. Because the vortex tilt and convective asymmetry are linked, and the convection is anchored to the low-level inflow (downtilt) side of the storm, the mean tilt of the vortex is slightly downshear whereas Reasor et al. (2004) find a mean tilt for adiabatic vortices to be 90° to the left of the shear. For similar reasons, the variation of the tilt associated with the quasi-mode is much smaller than for the adiabatic vortices in Reasor et al. (2004).

Prior conceptual models of eyewall updrafts have envisioned convective plumes initiating in the boundary layer and rising to the upper troposphere as the updrafts move cyclonically around the eye. The simulation of Bonnie suggests a somewhat different picture in which updrafts extend through the depth of the troposphere almost simultaneously upon initiation on the downtilt-right side of the eyewall and then rotate around the eye as vertically coherent columns of rising air. The timing and location of individual updrafts, while seemingly complex, have a surprisingly simple explanation. The updrafts form in association with mesovortices that are produced by the vorticity dynamics of the eyewall. As Schubert et al. (1999), Kossin and Schubert (2001), and Montgomery et al. (2002) have shown, the annulus of high potential vorticity associated with the eyewall is expected to support inflectional instabilities and, under certain conditions, breaks down to form steady mesovortices that rotate around the eye. These mesovortices often give rise to polygonal eyewalls and such structures are clearly evident in the Bonnie simulation. The mesovortices are relatively deep features that extend from the boundary layer up to ~5 km. The relationship between the mesovortices and updrafts are summarized in Fig. 18. The mesovortices are frequently associated with well-defined closed cyclonic circulations in the asymmetric flow (see updrafts A, D, E, and G in Fig. 16). In this situation, updrafts are initiated when the relative inflow associated with the environmental shear collides with the outflow associated with the mesovortices. The updrafts intensify as they move cyclonically around the eyewall just behind the mesovortices until they reach the downtilt direction and then begin to weaken as they rotate around to the downtilt-left side. The mesovortices are frequently maintained as they move around the uptilt side of the eyewall without an attendant updraft, and then initiate a new updraft upon entering the downtilt-right side. A variation on the initiation of the updrafts can also occur (not shown, but see updrafts B and F in Fig. 16) in which the mesovortex is associated with strong tangential flow perturbations either radially outside or inside of the mesovortex. Recent advances in geophysical

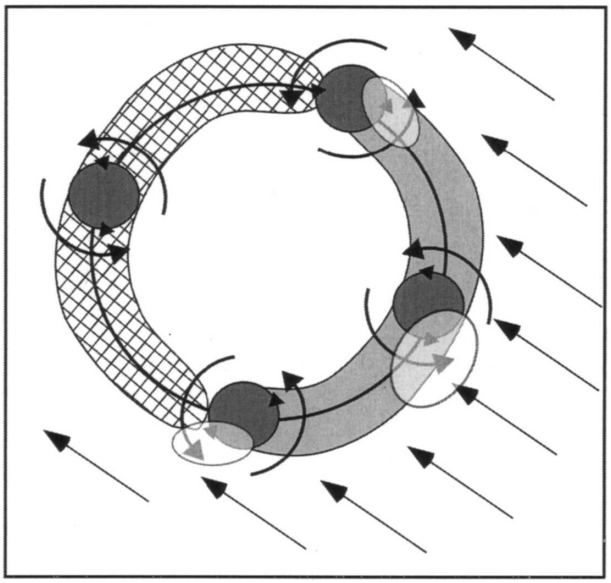

FIG. 18. Schematic diagram summarizing the interaction between eyewall mesovortices and the low-level inflow associated with the environmental wind shear. The elongated semicircular areas indicate where shear effects favor upward (light shading) and downward (cross hatching) motion. The relative flow associated with the environmental shear is indicated by the straight arrows, while the mesovortices and their local cyclonic circulations are indicated by darkly shaded circles and curved arrows. The semitransparent, lightly shaded ovals represent areas of enhanced low-level convergence and upward motion.

fluid dynamics explain the tendency of intense vortices to resist deformation and isolate their cores (e.g., McWilliams 1984; McIntyre 1989, 1993; Montgomery and Kallenbach 1997; McWilliams et al. 2003). These ideas find a natural application in the eyewall mesovortex problem. The anomalously high cyclonic relative vorticity found in an eyewall mesovortex together with its strong (local) potential vorticity gradient on its periphery tends to impede the low-level asymmetric inflow, causing enhanced convergence and upward motion radially outward of the mesovortex. After initiation of the updraft, the vorticity of the mesovortex increases by vortex tube stretching and the updraft shifts to the trailing side of the mesovortex. Thereafter, the evolution is similar to the first scenario above. Thus, the evolution of the updrafts results from an interplay between the mesovortex circulations and the wavenumber-1 forcing of upward motion associated with vertical wind shear.

In this study, we have focused on the distribution of vertical motion and on the roles played by environmental shear and eyewall mesovortices in forcing this vertical motion. Mesovortices are also likely important for exchanges of heat and momentum between the eyewall and the eye (Montgomery and Kallenbach 1997; Schubert et al. 1999; Kossin and Schubert 2001; Montgomery et al. 2002; Eastin 2003; Persing and Montgomery 2003). These processes will be examined using the simulation of Bonnie in a future study. The stronger updrafts associated with the mesovortices account for a large fraction of the vertical mass flux and condensation in the eyewall and are therefore major contributors to precipitation development. In Part II of this work (Braun 2006), a detailed water budget is calculated to examine the relative roles of vapor import in the radial inflow and evaporation from the ocean surface in supplying moisture to the inner core region as well as quantifying the contribution of eyewall precipitation processes to the development of stratiform precipitation outside the eyewall.

*Acknowledgments.* We thank Mark DeMaria for the SHIPS shear values for Bonnie and Paul Reasor and three anonymous reviewers for very helpful comments. This work was supported by Dr. Ramesh Kakar at NASA Headquarters with funds from the NASA CAMEX-4 and Precipitation Measurement Mission Science programs.

## REFERENCES

Bender, M. A., 1997: The effect of relative flow on the asymmetric structure in the interior of hurricanes. *J. Atmos. Sci.,* **54,** 703–724.

Bister, M., and K. A. Emanuel, 1998: Dissipative heating and hurricane intensity. *Meteor. Atmos. Phys.,* **55,** 233–240.

Black, M. L., R. W. Burpee, and F. D. Marks Jr., 1996: Vertical motion characteristics of tropical cyclones determined with airborne Doppler radial velocities. *J. Atmos. Sci.,* **53,** 1887–1909.

——, J. F. Gaache, F. D. Marks Jr., C. E. Samsury, and H. E. Willoughby, 2002: Eastern Pacific Hurricanes Jimena of 1991 and Olivia of 1994: The effect of vertical shear on structure and intensity. *Mon. Wea. Rev.,* **130,** 2291–2312.

Black, P. G., and F. D. Marks Jr., 1991: The structure of an eyewall mesovortex in Hurricane Hugo (1989). Preprints, *19th Conf. on Hurricanes and Tropical Meteorology*, Miami, FL, Amer. Meteor. Soc., 579–582.

Braun, S. A., 2002: A cloud-resolving simulation of Hurricane Bob (1991): Storm structure and eyewall buoyancy. *Mon. Wea. Rev.,* **130,** 1573–1592.

——, 2006: High-resolution simulation of Hurricane Bonnie (1998). Part II: Water budget. *J. Atmos. Sci.,* **63,** 43–64.

Carnevale, G. F., J. C. McWilliams, Y. Pomeau, J. B. Weiss, and W. R. Young, 1992: Rates, pathways, and end states of nonlinear evolution in decaying two-dimensional turbulence: Scaling theory vresus selective decay. *Phys. Fluids A,* **4,** 1314–1316.

Chen, Y., and M. K. Yau, 2001: Spiral bands in a simulated hurricane. Part I: Vortex Rossby wave verification. *J. Atmos. Sci.,* **58,** 2128–2145.

Corbosiero, K. L., and J. Molinari, 2003: The relationship between storm motion, vertical wind shear, and convective asymmetries in tropical cyclones. *J. Atmos. Sci.,* **60,** 366–376.

Drazin, P. G., and W. H. Reid, 1981: *Hydrodynamic Instability*. Cambridge University Press, 527 pp.

Dudhia, J., 1989: Numerical study of convection observed during the winter monsoon experiments using a mesoscale two-dimensional model. *J. Atmos. Sci.,* **46,** 3077–3107.

——, 1993: A nonhydrostatic version of the Penn State–NCAR Mesoscale Model: Validation tests and simulation of an Atlantic cyclone and cold front. *Mon. Wea. Rev.,* **121,** 1493–1513.

Eastin, M. D., 2003: Buoyancy of convective vertical motions in the inner core of intense hurricanes. Atmospheric Science Paper 744, Dept. of Atmospheric Science, Colorado State University, 160 pp.

Flatau, M., W. H. Schubert, and D. E. Stevens, 1994: The role of baroclinic processes in tropical cyclone motion: The influence of vertical tilt. *J. Atmos. Sci.,* **51,** 2589–2601.

Fovell, R. G., and Y. Ogura, 1988: Numerical simulation of a midlatitude squall line in two dimensions. *J. Atmos. Sci.,* **45,** 3846–3879.

Frank, W. M., and E. A. Ritchie, 1999: Effects of environmental flow upon tropical cyclone structure. *Mon. Wea. Rev.,* **127,** 2044–2061.

——, and ——, 2001: Effects of vertical wind shear on the intensity and structure of numerically simulated hurricanes. *Mon. Wea. Rev.,* **129,** 2249–2269.

Franklin, J. L., S. J. Lord, S. E. Feuer, and F. D. Marks Jr., 1993: The kinematic structure of Hurricane Gloria (1985) determined from nested analyses of dropwindsonde and Doppler radar data. *Mon. Wea. Rev.,* **121,** 2433–2451.

Fulton, J. D., 2001: Insights into the hurricane vortex using a high-resolution simulation of Hurricane Bob (1991). Masters thesis, Dept. of Atmospheric Science, Colorado State University, 84 pp.

Garratt, J. R., 1992: *The Atmospheric Boundary Layer*. Cambridge University Press, 316 pp.

Grell, G. A., J. Dudhia, and D. R. Stauffer, 1995: A description of the fifth-generation Penn State/NCAR Mesoscale Model (MM5). NCAR Tech. Note NCAR/TN-398+STR, 122 pp.

Heymsfield, G. M., J. Halverson, J. Simpson, L. Tian, and T. P. Bui, 2001: ER-2 Doppler radar (EDOP) investigations of the eyewall of Hurricane Bonnie during CAMEX-3. *J. Appl. Meteor.,* **40,** 1310–1330.

Holland, G., 1980: An analytic model of the wind and pressure profile in hurricanes. *Mon. Wea. Rev.,* **108,** 1212–1218.

Jones, S. C., 1995: The volution of vortices in vertical shear: Initially barotropic vortices. *Quart. J. Roy. Meteor. Soc.,* **121,** 821–851.

Jorgensen, D. P., 1984: Mesoscale and convective-scale characteristics of mature hurricanes. Part II: Inner core structure of Hurricane Allen (1980). *J. Atmos. Sci.,* **41,** 1287–1311.

——, E. J. Zipser, and M. A. LeMone, 1985: Vertical motions in intense hurricanes. *J. Atmos. Sci.,* **42,** 839–856.

Kaplan, J., and M. DeMaria, 2003: Large-scale characteristics of rapidly intensifying tropical cyclones in the North Atlantic basin. *Wea. Forecasting,* **18,** 1093–1108.

Kossin, J. P., and W. H. Schubert, 2001: Mesovortices, polygonal flow patterns, and rapid pressure falls in hurricane-like vortices. *J. Atmos. Sci.,* **58,** 2196–2209.

Kurihara, Y., M. A. Bender, and R. J. Ross, 1993: An initialization scheme of hurricane models by vortex specification. *Mon. Wea. Rev.,* **121,** 2030–2045.

Lewis, B. M., and H. F. Hawkins, 1982: Polygonal eye walls and rainbands in hurricanes. *Bull. Amer. Meteor. Soc.,* **63,** 1294–1300.

Manning, K. W., and P. L. Haagenson, 1992: Data ingest and objective analysis for the PSU/NCAR modeling system: Programs DATAGRID and RAWINS. NCAR Tech. Note NCAR/TN-376+IA, 209 pp.

Marks, F., Jr., 1985: Evolution of the structure of precipitation in Hurricane Allen (1980). *Mon. Wea. Rev.,* **113,** 909–930.

——, and P. G. Black, 1990: Close encounter with an intense mesoscale vortex within Hurricane Hugo (September 15, 1989). *Extended Abstracts, Fourth Conf. on Mesoscale Processes*, Boulder, CO, Amer. Meteor. Soc., 114–115.

——, R. A. Houze Jr., and J. F. Gamache, 1992: Dual-aircraft investigation of the inner core of Hurricane Norbert. Part I: Kinematic structure. *J. Atmos. Sci.,* **49,** 919–942.

McIntyre, M. E., 1989: On the Antarctic ozone hole. *J. Atmos. Terr. Phys.,* **51,** 2973–2994.

——, 1993: Isentropic distributions of potential vorticity and their relevance to tropical cyclone dynamics. *Tropical Cyclone Disasters: Proceedings of ISCU/WMO International Symposium,* Z. Zheng, G. Holland, and K. Emanuel, Eds., Peking University Press, 143–156.

McWilliams, J. C., 1984: The emergence of isolated coherent vortices in turbulent flow. *J. Fluid Mech.,* **146,** 21–43.

——, L. P. Graves, and M. T. Montgomery, 2003: A formal theory for vortex Rossby waves and vortex evolution. *Geophys. Astrophys. Fluid Dyn.,* **97,** 275–309.

Mlawer, E. J., S. J. Taubman, P. D. Brown, M. J. Iacono, and S. A. Clough, 1997: Radiative transfer for inhomogeneous atmosphere: RRTM, a validated correlated-k model for the longwave. *J. Geophys. Res.,* **102,** 16 663–16 682.

Montgomery, M. T., and L. J. Shapiro, 1995: Generalized Charney–Stern and Fjortoft theorems for rapidly rotating vortices. *J. Atmos. Sci.,* **52,** 1829–1833.

——, and R. J. Kallenbach, 1997: A theory for vortex Rossby waves and its application to spiral bands and intensity changes in hurricanes. *Quart. J. Roy. Meteor. Soc.,* **123,** 435–465.

——, V. A. Vladimirov, and P. V. Denissenko, 2002: An experimental study on hurricane mesovortices. *J. Fluid Mech.,* **471,** 1–32.

Nolan, D. S., and M. T. Montgomery, 2002: Nonhydrostatic, three-dimensional perturbations to balanced, hurricane-like vortices. Part I: Linearized formulation, stability, and evolution. *J. Atmos. Sci.,* **59,** 2989–3020.

Pagowski, M., and G. W. K. Moore, 2001: A numerical study of an extreme cold-air outbreak over the Labrador Sea: Sea ice, air–sea interaction, and development of polar lows. *Mon. Wea. Rev.,* **129,** 47–72.

Pasch, R. J., L. A. Avila, and J. L. Guiney, 2001: Atlantic hurricane season of 1998. *Mon. Wea. Rev.,* **129,** 3085–3123.

Persing, J., and M. T. Montgomery, 2003: Hurricane superintensity. *J. Atmos. Sci.,* **60,** 2349–2371.

Pu, Z., and S. Braun, 2001: Evaluation of bogus vortex techniques with four-dimensional variational data assimilation. *Mon. Wea. Rev.,* **129,** 2023–2039.

Raymond, D. J., 1992: Nonlinear balance and potential-vorticity thinking at large Rossby number. *Quart. J. Roy. Meteor. Soc.,* **118,** 987–1015.

Reasor, P. D., and M. T. Montgomery, 2001: Three-dimensional alignment and corotation of weak, TC-like vortices via linear vortex Rossby waves. *J. Atmos. Sci.,* **58,** 2306–2330.

——, ——, and L. D. Grasso, 2004: A new look at the problem of

tropical cyclones in vertical shear flow: Vortex resiliency. *J. Atmos. Sci.,* **61,** 3–22.

Ren, S., 1999: Further results on the stability of rapidly rotating vortices in the asymmetric balance formulation. *J. Atmos. Sci.,* **56,** 475–482.

Rogers, R., S. Chen, J. Tenerelli, and H. Willoughby, 2003: A numerical study of the impact of vertical shear on the distribution of rainfall in Hurricane Bonnie (1998). *Mon. Wea. Rev.,* **131,** 1577–1599.

Schubert, W. H., M. T. Montgomery, R. K. Taft, T. A. Guinn, S. R. Fulton, J. P. Kossin, and J. P. Edwards, 1999: Polygonal eyewalls, asymmetric eye contraction, and potential vorticity mixing in hurricanes. *J. Atmos. Sci.,* **56,** 1197–1223.

Shapiro, L. J., 1983: The asymmetric boundary layer flow under a translating hurricane. *J. Atmos. Sci.,* **40,** 1984–1998.

Wang, B., and X. Li, 1992: The beta drift of three-dimensional vortices: A numerical study. *Mon. Wea. Rev.,* **120,** 579–593.

Wang, Y., and G. J. Holland, 1996a: The beta drift of baroclinic vortices. Part I: Adiabatic vortices. *J. Atmos. Sci.,* **53,** 411–427.

——, and ——, 1996b: Tropical cyclone motion and evolution in vertical shear. *J. Atmos. Sci.,* **53,** 3313–3332.

——, and ——, 1996c: The beta drift of baroclinic vortices. Part II: Diabatic vortices. *J. Atmos. Sci.,* **53,** 3737–3756.

Weisman, M. L., and J. B. Klemp, 1986: Characteristics of isolated convective storms. *Mesoscale Meteorology and Forecasting*, Peter S. Ray, Ed., Amer. Meteor. Soc., 331–358.

Willoughby, H. E., 1998: Tropical cyclone eye thermodynamics. *Mon. Wea. Rev.,* **126,** 3053–3067.

——, F. D. Marks Jr., and R. J. Feinberg, 1984: Stationary and moving convective bands in hurricanes. *J. Atmos. Sci.,* **41,** 3189–3211.

Wu, L., S. A. Braun, J. Halverson, and G. Heymsfield, 2006: A numerical study of Hurricane Erin (2001). Part I: Model verification and storm evolution. *J. Atmos. Sci.,* **63,** 65–86.

Xiao, Q., X. Zou, and B. Wang, 2000: Initialization and simulation of a landfalling hurricane using variational bogus data assimilation scheme. *Mon. Wea. Rev.,* **128,** 2252–2269.

Zhang, D.-L., and E. Altshuler, 1999: The effects of dissipative heating on hurricane intensity. *Mon. Wea. Rev.,* **127,** 3032–3038.

——, Y. Liu, and M. K. Yau, 2002: A multiscale numerical study of Hurricane Andrew (1992). Part V: Inner-core thermodynamics. *Mon. Wea. Rev.,* **130,** 2745–2763.

Zhu, T., D.-L. Zhang, and F. Weng, 2004: Numerical simulation of Hurricane Bonnie (1998). Part I: Eyewall evolution and intensity changes. *Mon. Wea. Rev.,* **132,** 225–241.

Zou, X., and Q. Xiao, 2000: Studies on the initialization and simulation of a mature hurricane using a variational bogus data assimilation scheme. *J. Atmos. Sci.,* **57,** 836–860.